

The population of natural Earth satellites

Mikael Granvik^{a,b}, Jeremie Vaubaillon^c, Robert Jedicke^a

E-mail: mgranvik@iki.fi

^aInstitute for Astronomy, University of Hawaii, 2680 Woodlawn Drive,
Honolulu, HI 96822, U.S.A.

^bDepartment of Physics, P.O. Box 64, 00014 University of Helsinki, Finland

^cInstitut de Mécanique Céleste et de Calcul des Éphémérides, Observatoire
de Paris, 77 Avenue Denfert-Rochereau, F-75014 Paris, France

Submitted to *Icarus* on August 19, 2011

Accepted for publication on December 13, 2011

Manuscript pages: 63

Tables: 3

Figures: 29

Version: October 29, 2018

Proposed Running Head: The population of natural Earth satellites

Editorial correspondence to:

Mikael Granvik

Department of Physics

P.O. Box 64

00014 University of Helsinki

Finland

Phone: +358 (0)9 191 50751

Fax: +358 (0)9 191 50610

E-mail: mgranvik@iki.fi

Abstract

We have for the first time calculated the population characteristics of the Earth's irregular natural satellites (NES) that are temporarily captured from the near-Earth-object (NEO) population. The steady-state NES size-frequency and residence-time distributions were determined under the dynamical influence of all the massive bodies in the solar system (but mainly the Sun, Earth, and Moon) for NEOs of negligible mass. To this end, we compute the NES capture probability from the NEO population as a function of the latter's heliocentric orbital elements and combine those results with the current best estimates for the NEO size-frequency and orbital distribution. At any given time there should be at least one NES of 1-meter diameter orbiting the Earth. The average temporarily-captured orbiter (TCO; an object that makes at least one revolution around the Earth in a co-rotating coordinate system) completes (2.88 ± 0.82) rev around the Earth during a capture event that lasts (286 ± 18) d. We find a small preference for capture events starting in either January or July. Our results are consistent with the single known natural TCO, 2006 RH₁₂₀, a few-meter diameter object that was captured for about a year starting in June 2006. We estimate that about 0.1% of all meteors impacting the Earth were TCOs.

Key Words: NEAR-EARTH OBJECTS; SATELLITES, DYNAMICS; EARTH; IRREGULAR SATELLITES; METEORS

1 Introduction

In this work we provide the first study and characterization of the population of temporarily-captured natural Earth satellites (NES; Table 1 contains a list of all acronyms used in the paper) including their steady-state size-frequency distribution (SFD), capture probability as a function of the near-Earth-object (NEO) source population’s orbital elements, and their geocentric orbit residence-time distributions. The NES population provides a test of the NEO population statistics in a meteoroid size range that is not well-sampled by contemporary asteroid surveys—there are only three known NEOs with $H > 32$ as of Oct 22, 2011—and could provide a remote laboratory for detailed long-term studies of the physical properties of the smallest asteroids. The long-term future concept of a spacecraft mission to retrieve an entire meteoroid from Earth orbit would provide an unprecedented scientific opportunity.

NES	Natural Earth Satellite
SFD	Size-Frequency Distribution
NEO	Near-Earth Object
EMS	Earth-Moon System
TP	Test Particle
TC	Temporary Capture
TCO	Temporarily-Captured Orbiter
TCF	Temporarily-Captured Flyby
ISP	Intermediate Source Population
SP	Source Population

Table 1: List of acronyms.

Despite a large body of work on satellite capture by the gas giants, mainly Jupiter and Saturn, there has been surprisingly little published about the Earth’s natural satellites other than the Moon. The origin and evolution of the population of temporarily-captured irregular natural Earth satellites (NES) is entirely unknown.

To the best of our knowledge, the earliest paper mentioning NESs other than the Moon was Chant (1913). He explained that the great meteor procession witnessed in North America on Feb 9, 1913 “had been traveling through space, probably in an orbit about the sun, and that on coming near the earth

they were promptly captured by it and caused to move about it as a satellite.” A few years later Denning (1916) concluded that “the large meteors” that passed over Northern America in 1913 must have been temporary Earth satellites because they traveled 2600 miles in the atmosphere suggesting that the orbits were “concentric, or nearly concentric, with the Earth’s surface.”

Since about 1957 a large body of work has been carried out in the field of dynamics of low-altitude satellites with the main application being artificial spacecraft. Baker (1958) considered the possibility that artificial satellites “may be accompanied in their journey through space by certain ”natural” satellites.” He hypothesized that the heliocentric orbits of Earth-grazing meteors would become geocentric and elliptical as a result of atmospheric drag. In the next decade, Cassidy et al. (1965) suggested that the line of craters and hexahedrite meteorites associated with the Campo del Cielo craters in Argentina originated in a high-altitude break-up of a temporary Earth satellite in a decaying orbit. They also hypothesize that the North Chilean hexahedrites may be fragments of the same body which made one more revolution before coming to ground.

One line of studies on the dynamics of NESs was motivated by the hypothesis that the Moon would be the origin of the terrestrial tektites but a nontrivial transport mechanism was needed to explain their uneven distribution on the Earth’s surface (see, e.g., O’Keefe 1961). They are now thought to originate in terrestrial impact events.

Cline (1979) estimated the maximum speed of an object that can be captured by the Earth-Moon system (EMS) if the object has a very close encounter with the Moon. He concluded that in the four-body system (Sun-Earth-Moon-asteroid) an asteroid on a heliocentric orbit may be captured through a very close encounter with the Moon.

The first identification of an NES was only in the last decade. While Bagby (1969) provided direct and indirect evidence for electrically charged NESs, Meeus (1973) later revealed elementary misunderstandings and contradictions in the earlier work that completely refute any evidence of NESs. Tancredi (1997) discussed the origin of 1991 VG and suggested that this recurrently temporarily-captured object could be a piece of lunar ejecta formed by a large impact. The estimated absolute magnitude has a wide range ($26.7 < H < 29.0$) even when just considering slope parameters typical for natural objects with high albedos. However, the possibility that 1991 VG could be artificial has not yet been ruled out although this is an unlikely scenario due to the large projected area (G. Tancredi, personal communication).

Interestingly, 1991 VG is currently flagged as a Virtual Impactor by the Jet Propulsion Laboratory’s impact-monitoring system, SENTRY. Kwiatkowski et al. (2009) presented photometry of asteroid 2006 RH₁₂₀ ($H = 29.9 \pm 0.3$) which orbited the Earth within the Earth’s Hill sphere from July 2006 until July 2007. It has been concluded that it can not be a man-made object based on its low area-to-mass ratio (P. Chodas, personal communication) and high circular-polarization ratio and low albedo from radar observations (L. Benner, personal communication). The preliminary estimate for its diameter is > 2.3 m based on continuous-wave radar measurements.

We have not tested NEO orbits in the Minor Planet Center catalogue for temporary capture by the EMS, but have assumed that if such objects would exist they would have been reported in other publications. E.g., Kwiatkowski et al. (2009) give an extensive and detailed list of NES candidates, and argue that 2006 RH₁₂₀ is the only object certainly known to be a NES. Testing for past or future captures is not trivial — assuming that astrometric measurements are only available after the escape in the previous case — because the orbital uncertainties and long extrapolation intervals combined with the fractal nature of the orbit distribution for capturable objects (Murison 1989) might lead either to missing some captures or to false positive captures. The utility of adding possible NES candidates would thus be questionable for the purpose of estimating the validity of our results on the NES SFD. On the other hand, if there are observations of an object both before and after a capture it is likely that there also are some observations (or observers have at least attempted to get them) during the capture. It is likely that these events or their mere possibility would have been published in the literature.

The Earth’s quasi-satellites have some common characteristics with the NESs. (For a description of their dynamics see, e.g., Mikkola et al. (2006) and references therein.) The essential difference between satellites and quasi-satellites is that the NES orbit depends critically on the gravity of the EMS while the orbit of a quasi-satellite would hardly change if the EMS suddenly ceased to exist because it is orbiting the Sun on an Earth-like orbit in the vicinity of the Earth. Quasi-satellites thus form a subgroup of objects with co-orbital motion with respect to planets (objects on tadpole and horseshoe orbits form the other two subgroups). Based on the NEO model by Bottke et al. (2002), the steady-state population of Earth’s co-orbitals was estimated by Morais & Morbidelli (2002) to be around 13–19 objects with $H < 22$ and the length of the co-orbital motion episodes range from 25 kyr to 1 Myr in their integrations. The origin and evolution of Earth’s known co-orbitals

has recently been studied by Brasser & Wiegert (2008) who conclude that these objects should exist on Earth-like orbits for around 10kyr (note the discrepancy with Morais & Morbidelli) — three orders of magnitude shorter than the average lifespan of an NEO.

The general approach we have chosen to determine the NES SFD is to first calculate the capture probability as a function of the source population’s heliocentric orbital elements and then combine the probabilities with the best available NEO population models (Bottke et al. 2000, Bottke et al. 2002, Brown et al. 2002). The questions we will answer are:

- What is the steady-state population of temporary-captured NESs?
- What are the pre- and post-capture orbit distribution for NESs?
- How long do capture events last?
- How many orbits does an NES typically complete before escaping the EMS?
- What fraction of NESs impact the Earth and Moon while captured?
- What are the orbit characteristics of an NES?
- Can an NES become a temporary Moon satellite?
- Are capture events equally likely to happen throughout the year?

2 Definitions and methods

2.1 Definition for temporary capture

Following Kary & Dones (1996), we use a two-fold definition for a temporary satellite capture by a planet (or any object orbiting the Sun including the Moon) by requiring simultaneously that

1. the planetocentric Keplerian energy $E_{\text{planet}} < 0$, and that
2. the planetocentric distance is less than three Hill radii for the planet in question (e.g., for the Earth $3R_{H,\oplus} \sim 0.03 \text{ AU}$).

We call a test particle (TP) a temporarily-captured orbiter (TCO) if it makes at least one full revolution around the planet in a co-rotating frame while being captured (the line from the planet to the Sun is fixed in this coordinate system). If a temporarily-captured TP fails to complete a full revolution around the planet we call it a temporarily-captured fly-by (TCF). 1991 VG was neither a TCF nor a TCO during its 1991-1992 encounter (due to energy and/or distance criteria; see Fig 1 in Tancredi 1997) whereas 2006 RH₁₂₀ was a TCO during its 2006-2007 encounter. The practical limit to the minimum duration of a TCF is two integration steps because a single integration step does not allow us to estimate the capture duration.

We count the number of revolutions by recording the longitudinal angle traversed during the capture. The longitude is measured in a co-rotating ecliptic coordinate system where the line connecting the planet and the Sun forms the line of reference. At every timestep we add the difference between the current and the previous longitude to a counter which results in a negative angle for retrograde orbits (as seen from the north ecliptic pole) and a positive angle for prograde orbits. A horseshoe-type orbit would result in less than one apparent revolution being recorded regardless of how many loops the object completes. 2000 SG₃₄₄ did not qualify as a TCO during its Earth encounter in 2000.

2.2 Generation of initial conditions for test particles

In what follows we describe the technique we use to generate initial orbits for TPs in a volume that harbors NEOs shortly before their capture by the EMS. The fundamental idea is that TPs that can get captured by the EMS are constrained to a fairly small volume in the heliocentric orbital elements (semimajor axis a_h , eccentricity e_h , inclination i_h) space centered around the Earth’s orbit. We will call the population of capturable NEOs the intermediate source population (ISP).

We start by drawing a random (a_h, e_h, i_h) triplet from a uniform distribution just slightly larger than the volume harboring “capturable” orbits ($0.87 \text{ AU} < a_h < 1.15 \text{ AU}$, $0 < e_h < 0.12$, and $0^\circ < i_h < 2.5^\circ$). We then draw a random longitude of node, Ω_h , argument of perihelion, ω_h , and mean anomaly, M_{0h} triplet each from a uniform distribution in the interval $[0, 2\pi]$ radians. The intervals for (a_h, e_h, i_h) were selected empirically to ensure that they span the complete phase space of initial conditions that can result in temporary captures. In order to average over different geometries between

the asteroid, the Earth, the Moon, and the Sun, the epoch is randomly selected from a uniform distribution spanning the ~ 19 -year Metonic Cycle. The Metonic Cycle is the period over which a given lunar phase repeats at the same time of the year and it is accurate to a couple of hours.

We add the generated trial orbit to the sample of TPs to be integrated thru the EMS if

1. the TP’s geocentric distance is between 4 and 5 Earth’s Hill radii (0.04–0.05 AU) at the epoch,
2. the TP has a slow-enough geocentric speed $v_g(r) < v_e(r) + 2.5 \text{ km s}^{-1}$ where $v_e(r)$ is the escape speed at geocentric distance r , and
3. the direction angle $\theta < 130^\circ$, the angle between the instantaneous geocentric velocity vector and the instantaneous TP-centric position vector of the Earth (see Fig. 1).

In Sect. 3.2 we will explicitly verify that the cuts imposed on the distribution of integrated TPs do not reject candidates that might evolve into TCOs on this pass thru the EMS. All trial orbits are counted and the result stored so that we can calculate the capture probability as a function of (a_h, e_h, i_h) .

This ‘brute-force’ technique is feasible in our case only because the likelihood of a close Earth encounter is highest for Earth-like orbits with $a_h \sim 1 \text{ AU}$, $e_h \sim 0$, and $i_h \sim 0$. Approximately one in 1,000 of the generated random orbits (also known as state vectors) fulfill all requirements. To generate 10^7 TP orbits we thus need to generate “only” about 10^{10} trial orbits. Appendix A describes a generic technique that can be used for generating orbits in any situation when the (a_h, e_h, i_h) distribution and the heliocentric position vector $(x_h, y_h, z_h)_{t_0}$ distribution are known.

2.3 Integrations

The orbit of each TP was integrated using the Gram, Bulirsch and Stoer algorithm (Stoer & Bulirsch 2002) starting with the initial conditions described in Sect. 2.2. Only gravitational perturbations from the point-like masses of the Sun, the eight planets and the Moon were taken into account. We stress the fact that atmospheric drag was not included in the integrations. We did not integrate the perturbers’ orbits but instead we obtained the positions from a special version of IMCCE’s INPOP planetary ephemerides (Fienga

et al. 2008). The integrations were performed using between 8 and 1,024 cores on the Jade supercluster (SGI Altix ICE 8200) located at the Centre Informatique National de l’Enseignement Supérieur (CINES) in France.

Each TP was integrated separately and for at least 2 kdays to allow almost co-moving objects to approach the Earth. TPs that were still captured after 2 kdays were integrated until they escaped the EMS. The integration was stopped if the TP collided with the Earth or the Moon (i.e., its geocentric or lunacentric distance were $\leq 4.25 \times 10^{-5}$ AU or $\leq 1.16 \times 10^{-5}$ AU corresponding roughly to the Earth’s and Moon’s radius, respectively). The orbital elements of the TP with respect to both the Earth and the Moon were computed at each integration step — the length of which varied from a fraction of a day to tens of days depending on the automated optimization — and stored if $E_{\oplus} < 0$ or $E_{\text{D}} < 0$ (see Sect. 2.1).

2.4 NES pre-capture heliocentric orbit-density distribution

Let the source population’s (i.e. NEOs’) debiased SFD and heliocentric orbit-density distribution be represented by $N_{\text{NEO}}(H)$ and $R_{\text{NEO}}(a_h, e_h, i_h)$, respectively.

The heliocentric orbit-density distribution for the subset of objects in the ISP that will eventually evolve into the target population is

$$R'_{\text{ISP}}(a_h, e_h, i_h) = E_{\text{gen}}(a_h, e_h, i_h) \times E_{\text{capt}}(a_h, e_h, i_h) \times R_{\text{NEO}}(a_h, e_h, i_h) \quad (1)$$

where $E_{\text{gen}}(a_h, e_h, i_h)$ is the efficiency for generating initial conditions to be integrated, $E_{\text{capt}}(a_h, e_h, i_h)$ is the capture efficiency among the integrated orbits, and the prime indicates that R'_{ISP} is a subset of the heliocentric orbit-density distribution for the ISP, R_{ISP} .

The generation efficiency is defined as

$$E_{\text{gen}}(a_h, e_h, i_h) = \frac{N_{\text{int}}(a_h, e_h, i_h)}{N_{\text{aei}}(a_h, e_h, i_h)} \quad (2)$$

where $N_{\text{int}}(a_h, e_h, i_h)$ is the number of TPs that were integrated (see Sect. 2.2) and $N_{\text{aei}}(a_h, e_h, i_h)$ is the total number of trial orbits.

The capture efficiency of the integrated TP orbits is defined as

$$E_{\text{capt,int}}(a_h, e_h, i_h) = \frac{N_{\text{capt}}(a_h, e_h, i_h)}{N_{\text{int}}(a_h, e_h, i_h)}, \quad (3)$$

where $N_{\text{capt}}(a_h, e_h, i_h)$ is the number of captured TPs.

The orbit-density distribution can then be reduced to

$$R'_{\text{ISP}}(a_h, e_h, i_h) = \frac{N_{\text{capt}}(a_h, e_h, i_h)}{N_{\text{aei}}(a_h, e_h, i_h)} \times R_{\text{NEO}}(a_h, e_h, i_h) \quad (4)$$

$$= E_{\text{capt}}(a_h, e_h, i_h) \times R_{\text{NEO}}(a_h, e_h, i_h). \quad (5)$$

Note that $E_{\text{capt}}(a_h, e_h, i_h)$ is defined only when $N_{\text{aei}}(a_h, e_h, i_h) \neq 0$, which sets an upper limit on the resolution of the binning assuming a fixed number of test particles. In practice, we want $N_{\text{aei}}(a_h, e_h, i_h) \gg 1$ to minimize the statistical error on the results. It is also important to ensure that $N_{\text{aei}}(a_h, e_h, i_h)$ is essentially constant over the relevant volume or, alternatively, correct for an uneven distribution in (a_h, e_h, i_h) space. In our case the technique used for generating TP orbits ensures that the distribution in (a_h, e_h, i_h) space is uniform.

2.5 Steady-state size-frequency distribution

A relatively well-known result in statistical physics is that in the steady-state scenario the size, N , mean lifetime, \bar{L} , and flux rate, F , into (or out of) the population are related by

$$N = F\bar{L}. \quad (6)$$

Thus, the NES steady-state SFD, $N_{\text{NES}}(H)$, can be determined from $F_{\text{NES}}(H)$ and \bar{L}_{NES} . The latter can be obtained from orbital integrations by calculating the average time that an object fulfills the conditions of being an NES. We determined F_{NES} using two different methods as described in the following two subsections.

2.5.1 NES Flux determination (following Morais & Morbidelli 2002)

In this method the flux into the NES population is obtained from

$$F_{\text{NES1}}(H) = r_{\text{ISP}} N'_{\text{ISP}}(H), \quad (7)$$

where r_{ISP} is the fractional decay rate from the ISP into the NES population and $N'_{\text{ISP}}(H)$ is the number of objects in the ISP that will eventually evolve into the NES population:

$$N'_{\text{ISP}}(H) = N_{\text{NEO}}(H) \iiint R'_{\text{ISP}}(a_h, e_h, i_h) da_h de_h di_h. \quad (8)$$

The triple integral is a scaling factor that is directly proportional to the capture efficiency and can be calculated by integrating over Eq. 4. Note that the steady-state SFD for the intermediate source population $N'_{\text{ISP}}(H)$ is not equal to the steady-state SFD for the target population $N_{\text{NES}}(H)$ because of the different average lifetimes in the two regions.

To calculate r_{ISP} we imagine that we suddenly stopped feeding the ISP. The N'_{ISP} objects in the ISP would start decaying into the NES population at a rate

$$\frac{dN'_{\text{ISP}}}{dt} = -r_{\text{ISP}}(t) N'_{\text{ISP}}. \quad (9)$$

For a sufficiently short time interval at some time t we can assume that the fractional decay rate is constant, $r_{\text{ISP}}(t) = r_{\text{ISP}}$, and integrate the equation to obtain

$$N'_{\text{ISP}}(t) = N'_{\text{ISP}} \exp[-r_{\text{ISP}}t], \quad (10)$$

where $N'_{\text{ISP}}(t)$ is the number of objects left in the ISP at time t that will eventually evolve into the NES population. The fractional decay rate can thus be obtained by fitting a straight line to $\ln[N'_{\text{ISP}}(t)]$ over some short time interval during which r_{ISP} can be assumed constant. With both of the right-hand terms in Eq. 7 determined we can then calculate F_{NES1} .

2.5.2 NES Flux determination (Alternative)

The second method for estimating the flux into the NES population is based on the assumption that the flux from the source population into the ISP, $F_{\text{ISP}}(H)$, is proportional to the flux from the ISP into the NES population, $F_{\text{NES}}(H)$. The size of the steady-state population in the ISP, $N_{\text{ISP}}(H)$, can be estimated using the NEO model and knowledge of how the TP orbits were generated. The average lifetime of the objects in the ISP, \bar{L}_{ISP} , is measured from the TP integrations. The flux into the ISP is then

$$F_{\text{ISP}}(H) = \frac{N_{\text{ISP}}(H)}{\bar{L}_{\text{ISP}}}. \quad (11)$$

From the integrations we can estimate the fraction $f_{\text{NES/ISP}}$ of objects in the ISP that eventually reach the NES population and then the flux into the NES population as a function of the absolute magnitude is

$$F_{\text{NES2}}(H) = f_{\text{NES/ISP}} F_{\text{ISP}}(H). \quad (12)$$

3 Results and discussion

Unless otherwise specified this section applies to TCOs only.

3.1 The nominal model and the barycentric model

To investigate the role of the Moon in capturing temporary satellites we used two different dynamical models: 1) the *nominal model* in which the Earth and Moon are treated as separate perturbers and 2) the *barycentric model* where the Earth and the Moon are combined into a single perturber located at the EMS barycenter with the combined mass of the Earth and the Moon (~ 1.012 Earth masses).

Changing the location of the Earth’s mass from the geocenter to the barycenter has a negligible effect on the geometry because the difference between the geocenter and the EMS barycenter is only about 3×10^{-5} AU or roughly a thousandth of the geocentric distance to the TP’s initial locations. The apparent location of the Earth as seen from an object at a geocentric distance of 0.04 AU will not change by more than $\sim 0.043^\circ$.

3.2 Test particle generation and integration

A possible concern with this study might be that the generated TPs that were integrated through the EMS do not span the entire range of ‘capturable’ orbits. In this case our results would imply only a lower limit to the TCO rate. However, Figs. 2-4 illustrate that our generated TPs expand *beyond* the necessary ranges. Specifically, Fig. 2 shows that the generated heliocentric (a, e, i) distributions for the TPs that evolve into TCOs occupy a smaller volume than all the integrated TPs. Figure 3 shows that the initial geocentric speed of the generated TPs spans a much wider range of values than that of the objects that become TCOs which typically have $v_g \lesssim 2.2 \text{ km s}^{-1}$. Finally, the direction-angle distribution at the generation epoch does not have a cut-off at $\theta_{\text{init}} = 90^\circ$ as might be naively expected, but extends to $\theta_{\text{init}} \sim 125^\circ$ — still below our $\theta_{\text{init}} < 130^\circ$ criterion in generating the TPs (see Fig. 4). The reason some TCOs that are initially moving away from the Earth turn around and approach the Earth is not that they are attracted by the Earth’s gravity: even when the gravity of all the planets and the Moon are excluded from the integrations these initially outward-moving TCOs still appear to turn around and move towards the Earth. Hence, the behavior is due to the

**Bulk properties of the generated
test particles and captured objects**

N_{tot}	9, 346, 396, 100
N_{int}	10, 000, 000
Nominal model	
$N_{\text{TCF,short}}$	209, 917
$N_{\text{TCF,long}}$	23, 771
N_{TCO}	18, 096
\bar{L}_{TC}	(62.2 ± 1.3) d
$\bar{\tau}_{\text{TC}}$	(0.383 ± 0.059) rev
\bar{L}_{TCO}	(286 ± 18) d
$\bar{\tau}_{\text{TCO}}$	(2.88 ± 0.82) rev
Fraction of TCOs with	
$\tau_{\text{TCO}} > 2.88$ rev	11%
$\tau_{\text{TCO}} > 5$ rev	3.4%
$\tau_{\text{TCO}} > 50$ rev	0.1%
TCO > 271 d	26%
TCO > 365 d	15%
TCO > 3650 d	0.1%
Barycentric model	
$N_{\text{TCF,short}}$	320, 748
$N_{\text{TCF,long}}$	34, 843
N_{TCO}	4, 494
\bar{L}_{TC}	(53.76 ± 0.11) d
$\bar{\tau}_{\text{TC}}$	(0.21751 ± 0.00037) rev
\bar{L}_{TCO}	(334.6 ± 1.7) d
$\bar{\tau}_{\text{TCO}}$	(1.1280 ± 0.0019) rev

Table 2: N_{tot} is the total number of generated TPs, N_{int} is the number of integrated TPs, $N_{\text{TCF,short}}$ is the number of TCFs making less than half a revolution, $N_{\text{TCF,long}}$ is the number of TCFs making more than half a revolution but less than one, N_{TCO} is the number of TPs making more than one revolution, \bar{L}_{TC} is the average duration of a temporary capture, $\bar{\tau}_{\text{TC}}$ is the average number of revolutions during a temporary capture, \bar{L}_{TCO} is the average lifetime of a TCO, and $\bar{\tau}_{\text{TCO}}$ is the average number of revolutions made by a TCO during the time of capture.

mutual geometry of the Earth’s and the asteroids’ orbits. We see that the v_g distribution is shifted towards faster speeds in the nominal model compared to the barycentric model while the distribution of θ_{init} is wider for the nominal model. In other words, the Moon allows faster objects to be captured over a wider range of initial direction angles.

About 20% of all TCFs and TCOs are captured on multiple occasions during the 2-kday integration and for 14 TPs the multiple events include TCO-level captures. While these events represent an insignificant fraction of the capture events, to avoid double counting in the analysis we only take into account the first TCO capture for any TP. When a TP is captured and released to the NEO population it again becomes part of the input NEO population.

Some bulk parameters for the generated particles and capture events that lasted longer than one integration step are listed in Table 2. Note that the distribution of the TCO lifetimes and their number of revolutions have extremely long tails in the nominal model (Fig. 5). For example, the longest capture event lasts 325,039 d (or about $1,200 \times \bar{L}_{\text{TCO}}$) during which the the TP makes 14,801 rev around the Earth (about $5,140 \times \bar{\tau}_{\text{TCO}}$).

Our TCO distribution is not biased by a truncation in the integration time. More than 99.9% of all TCOs complete their first revolution less than ~ 400 days after the generation epoch (Fig. 6) and all TPs were integrated for at least 2 kdays. The TPs that were captured after 2 kdays were integrated until they escaped.

3.3 Capture probability and capture mechanism for temporarily-captured orbiters

Figure 2 shows a subset the initial orbital elements (a_h , e_h , i_h , and longitude of perihelion ϖ_h) of a representative sample of all integrated TPs overplotted by those resulting in TCOs. The most striking feature is the almost complete lack of TCOs that are initially on orbits with $a_h \sim 1$ AU. This is neither due to a too short integration time which would prevent the slowest TPs to reach the target region (Fig. 6) nor can it be explained by the intrinsically higher impact probability for $a_h \sim 1$ AU orbits because the impact probability is only of the order of 10^{-4} and there should be plenty of objects replenishing the wake left by the impactors (Fig. 7). Furthermore, the gap in semimajor axis cannot be explained by very-Earth-like orbits not reaching the capture

volume near L_1 or L_2 , because the width of the gap is independent of eccentricity. We think that the single most important explanation for the gap in the heliocentric semimajor-axis distribution is related to few-body dynamics: when a TP approaches the EMS on a near-circular orbit with $a_h \sim a_\oplus$ it often follows either a horseshoe orbit or a quasi-satellite orbit and cannot get close enough to the EMS for capture (see, e.g., Chapter 3.13 in Murray & Dermott 1999). To verify this hypothesis, we first examined the Jacobi constant as a function of a_h

$$C = \frac{1}{2}v^2 + U(x, y, z), \quad (13)$$

where both the speed v and the potential $U(x, y, z)$ are given in the rotating frame (Fig. 8). We define two C - a_h regions in the figure: 'A' representing TPs that become TCOs and 'B' representing TPs that do not become TCOs even though the objects in 'B' have the same value of the Jacobi constant as the TPs in 'A'. The figure shows we can rule out the possibility that TPs with $a_h \sim a_\oplus$ have too small a C to enter the EMS through L_1 or L_2 because the range in C is identical in both the 'A' and 'B' regions and there are many TCOs in 'A'. We then randomly selected 100 TPs from both regions with the additional constraint that $i_h < 1^\circ$, and integrated the subsets of TPs for 500 yr. In region 'A' we find evidence for one horseshoe orbit whereas in region 'B' we find evidence for about 16 quasi-satellite orbits and 17 horseshoe orbits. Thus we conclude that roughly one third of the TPs in region 'B' are prevented from close encounters with the EMS.

Figure 9 shows the TCO capture probability, $E_{\text{capt}}(a_h, e_h, i_h)$, as a function of their pre-capture heliocentric orbital elements. The wings of the (a_h, e_h) distribution follow the perihelion $q_h = 1$ AU and aphelion $Q_h = 1$ AU lines indicating that a TP on an orbit allowing a grazing encounter with the Earth's orbit may lead to the TP becoming a TCO whereas Earth-like $a_h \sim 1$ AU orbits in general are not necessarily capturable even with fairly low eccentricities (cf. Carusi & Valsecchi 1979). The logarithmic scale in Fig. 9 may be misleading since most of the capture probability is focused in the 0.01 AU semi-major axis ranges between 0.98-0.99 AU and 1.01-1.02 AU with a slight preference for a non-zero eccentricity in the range 0.01-0.02. Although Figs. 2 and 9 suggest that the highest capture probability is achieved when $q_h \sim q_\oplus = 0.983$ AU or $Q_h \sim Q_\oplus = 1.017$ AU and $\varpi_h \sim \varpi_\oplus$ — that is, when line of apsides between the Earth and the TP are aligned and their perihelion and aphelion distances are similar thus resulting in co-linear ve-

locity vectors for the Earth and the TP — the reality is more complicated. Figure 10 shows that the maximum of the capture probability is bifurcated (or bimodal) in q and Q and extended in ϖ_h . The reason for the bifurcation is, to the best of our knowledge, currently unknown but we presume that it is a feature of the elliptic four body problem.

When comparing the capture probability distribution with the orbital elements of known NEOs in Fig. 9 bear in mind that the capture probability is a function of the TP’s orbital elements when they have a geocentric distance of 0.04–0.05 AU whereas the orbital elements for the known NEOs in the figure have not been filtered based on their geocentric distance. The orbital elements of the known NEOs would change through planetary perturbations if they were integrated until they had similar geocentric distances as the TPs. Despite the slight inconsistency, the one confirmed former TCO, 2006 RH₁₂₀, still lies in a region that has a non-zero capture likelihood so that it could be captured again in the future.

A comparison with the barycentric model underscores the importance of the Moon for the capture events as shown in Fig. 11. The wings in the (a_h, e_h) distribution clearly require the presence of the Moon but also the width in a_h of the non-zero capture probability region increases dramatically when the Moon is included in the integrations. Moreover, the results for the barycentric model indicate that the presence of the Moon was of critical importance in the capture of 2006 RH₁₂₀ because its heliocentric elements prior to capture (on 2006 March 21 UT) at a geocentric distance of about 0.047 AU — $a_h \sim 0.954$ AU, $e_h \sim 0.051$, and $i_h \sim 0.565^\circ$ — would have placed it outside the capture region for the barycentric model. The comparison between the capture probability for the nominal and barycentric models indicates that one should be wary of results that utilized a barycentric model to analyze temporary satellite captures by the Earth (c.f., Tancredi 1997).

The capture regions for slow-moving TCOs — the region where the geocentric orbital energy for TCOs first turns negative — are in the vicinity of the Sun-Earth Lagrange equilibrium points L_1 and L_2 with roughly equal shares for both regions (for illustrations and detailed explanations of the dynamics, see, e.g., Baoyin et al. 2010, Iwasaki & Ohtsuki 2007, and references therein). The L_1 and L_2 as derived for the circular restricted three-body problem should only be understood as approximate reference points when interpreting Fig. 12 because the fundamental problem with satellite captures by the EMS is the elliptic four-body problem.

Retrograde geocentric orbits are preferred at the time of capture with a

share of approximately 2:1 (Fig. 12). Note that some 90% of the objects appear to move in a retrograde fashion in the rotating frame due to their slow geocentric angular velocity and the fairly large apparent angular velocity of the Sun. Not a single TP is *captured* by lowering the geocentric velocity via extremely close lunar fly-bys so we conclude that even though the mechanism by Cline (1979) might be theoretically sound it is not important in realistic capture scenarios. Among our integration results there is, however, at least one example of a very close lunar fly-by *after* the initial capture that eventually lead to a very long-lived TCO.

The volume of (a_h, e_h, i_h) -space harboring capturable TPs shrinks when the Moon is omitted from the integrations in our barycentric model. Comparing Figs. 2 and 13 shows that presence of the Moon expands the semimajor-axis range while narrowing the inclination range of the pre-capture TCO heliocentric orbits. Although conventional wisdom suggests that the Moon’s orbit is the primary reason for the lack of long-lived TCOs, it is simultaneously the presence of the Moon that increases the capture probability by allowing faster objects to be captured (Table 2; c.f. Cline 1979).

The longitude of perihelia for TCOs’ pre-capture orbits are preferably aligned with that of the Earth ($\sim 103^\circ$). We interpret the Earth-like perihelion longitudes to be a geometric preference rather than due to secular perturbations because the integrations typically last for only a few years, too short a time interval for secular perturbations to modify the heliocentric orbit distribution enough to explain the results. The longitude of perihelia preference manifests itself as an inconstant TCO capture probability throughout the year. Whereas the generation epochs are uniformly distributed over a year the time-of-capture distribution has two annual peaks — one in late January and one in late July (Fig. 14). The peaks occur about 1–2 weeks after Earth’s perihelion in January and aphelion in July (c.f., the alignment of the TCOs’ longitude of perihelia with that of the Earth’s). The amplitude of the variation is $\lesssim 20\%$ when the data is binned with a resolution of about 7.3 days. Note that the single verified TCO, 2006 RH₁₂₀, was, by our definition of a TCO, captured in June. A typical TCO will thus get captured at Earth’s perihelion or aphelion and, since the distribution of the duration of capture has a peak at 180 days (see Fig. 5), escape at the following Earth aphelion or perihelion, respectively. A similar alignment of the capture and escape times has also been observed for temporary satellite captures by Jupiter (Tancredi et al. 1990).

3.4 Heliocentric orbit density for TCOs in the ISP

To calculate the heliocentric orbit-density distribution $R'_{\text{ISP}}(a, e, i)$ for TPs in the ISP that will eventually evolve into the NES population we use the Bottke et al. (2002) NEO model orbit distribution $R_{\text{NEO}}(a_h, e_h, i_h)$ (Fig. 15). A limitation with using this R_{NEO} model is that its resolution is much lower than the resolution we obtain for the raw capture probability R_{capt} — we use 4 bins from the NEO model whereas the same volume contains 20,000 bins in R_{capt} . Thus, our knowledge of the heliocentric pre-capture orbit-density distribution for TCOs is limited by the lack of a high-resolution NEO orbit-distribution model.

3.5 Steady-state size-frequency distribution of temporarily-captured orbiters

The TCO steady-state SFD, i.e., the number of TCOs as a function of their absolute magnitude ($N_{\text{TCO}}(H)$), is determined by the NEO SFD, the flux into the TCO population, $F_{\text{TCO1}} = F_{\text{NES1}}$ and $F_{\text{TCO2}} = F_{\text{NES2}}$ as discussed in sect. 2.5, and the average TCO lifetime $\bar{L}_{\text{TCO}} = \bar{L}_{\text{NES}}$ (obtained directly from the integrations). Thus, we require an independent measurement of the NEO SFD in order to determine the TCO SFD.

Motivated by the fact that the only verified TCO, 2006 RH₁₂₀, was a few meters in diameter we expected that it was important to use a NEO SFD relevant to meter-scale objects ($H \sim 30$). We used two of the available SFDs, Rabinowitz et al.'s (2000) $N_{\text{Ra00}}(H) \propto 10^{0.7H}$ valid for $24 < H < 31$, and Brown et al.'s (2002) estimate for Earth impactors $N_{\text{Br02}}(H) \propto 10^{(0.540 \pm 0.016)H}$ valid for $22 < H < 30$. Another independent estimate for the NEO SFD comes from the analysis of the lunar impactors (see, e.g., Werner et al. 2002) which is about an order of magnitude below the estimate for NEOs with $H \sim 30$ by Rabinowitz et al. (2000) but agrees well with the estimate by Brown et al. (2002).

Considering that we used the Bottke et al. (2000) model for the NEO orbit distribution we also used their SFD of $N_{\text{Bo00}}(H) \propto 10^{(0.35 \pm 0.02)(H-H_0)}$ which is strictly valid for $15 < H < 22$ but we simply extrapolated it to the size range of interest. At $H = 33$ the raw models differ in the predicted number of objects by several orders of magnitude. In order to bridge the gaps in H between the different SFDs, we scale the absolute number of objects in the source population (that is, in the NEO population) to $N_0 = N(H = 24)$ which is

obtained through extrapolation of the Bottke et al. (2000) model $N_{\text{B00}}(H = 24) = C_{\text{NEO}} 10^{(0.35 \pm 0.02)(H - 13.0)} = 13.26 \times 10^{(0.35 \pm 0.02) \times 11.0} = 93874 \pm 47553$ (cf. Jedicke et al. 2002). It turns out that the differences between using the absolute numbers by Rabinowitz et al. (2000) and the broken power law described above are negligible compared to the other error sources; the flux at $H = 30$ is different by a factor of about two. We chose to use the broken power law because the SFD by Rabinowitz et al. (2000) is not readily available in a

Measured and published parameters		
C_{NEO}		13.26
$n_{\text{ISP}} \equiv N_{\text{int}}$		10^7
$ r_{\text{ISP}} $	$(1.35575 \pm 0.00085) \times 10^{-2}$	d^{-1}
R_{ISP}		4.0×10^{-5}
$\iiint R'_{\text{ISP}}(a_h, e_h, i_h) da_h de_h di_h$		2.972×10^{-10}
\bar{L}_{ISP}	$(3.991 \pm 0.022) \times 10^1$	d
Derived parameters		
$N_0 = N(H = 24)$		$(9.3874 \pm 4.7553) \times 10^4$
$f_{\text{ISP/NEO}}$		$(1.06993 \pm 0.00034) \times 10^{-3}$
$N_{\text{ISP}}(H = 24)$		$(4.02 \pm 0.54) \times 10^{-3}$
$F_{\text{ISP}}(H = 24)$		$(1.007 \pm 0.136) \times 10^{-4} \text{ d}^{-1}$
$f_{\text{TCO/ISP}}$		$(1.810 \pm 0.013) \times 10^{-3}$
$F_{\text{TCO1}}(H = 24)$		$(3.78 \pm 1.92) \times 10^{-7} \text{ d}^{-1}$
$F_{\text{TCO2}}(H = 24)$		$(1.82 \pm 0.25) \times 10^{-7} \text{ d}^{-1}$

Table 3: Bulk parameters of the NEO and TCO populations. C_{NEO} is the constant in the power-law SFD and has been estimated assuming that there are 66 NEOs in the size range $13 < H_V < 15$ by Bottke et al. (2000), n_{ISP} is the number of TPs in the ISP, r_{ISP} is the fractional decay rate from the ISP to the TCO population, R_{ISP} is the fraction of all NEOs that are in the region from which TPs are generated, \bar{L}_{ISP} is the average lifetime of a TP in the ISP, N_0 is the extrapolated number of NEOs with $H = 24$, $N_{\text{ISP}}(H = 24)$ is the number of objects with $H = 24$ in the ISP in the steady-state scenario, $f_{\text{ISP/NEO}}$ is the fraction of NEOs generated that qualify for the ISP, $F_{\text{ISP}}(H = 24)$ is the flux of objects with $H = 24$ into the ISP, $f_{\text{TCO/ISP}}$ is the ratio of objects in the ISP that enter the TCO population, and F_{TCO1} and F_{TCO2} are the flux of objects into the TCO region from the ISP calculated using two different methods.

functional form but only as a plot.

We note that the constant C_{NEO} was estimated 11 years ago when 53 NEOs in the size range $13 < H < 15$ were known (Bottke et al. 2000). The completeness level for that size range was assumed to be 80% based on the completeness level for NEOs with $H < 16$ which in turn was based on data from 1996 to 1998. The total population of NEOs in the size range $13 < H < 15$ was therefore assumed to be 66. During the past 11 years the number of NEOs with $H < 15$ has grown to 55, but eight of them have been discovered since April 2000 (the last one in 2004). These facts lead us to conclude that although some objects have been discarded from the sample due to, for example, improved, fainter absolute magnitudes, the total number of NEOs in the size range is smaller than anticipated in 2000. The constant C_{NEO} may thus be up to about 20% smaller than estimated by Bottke et al. (2000). We will nevertheless use the original value for the constant since its error is relatively small.

Table 3 lists all parameters that are used when computing the fluxes and, further, the SFDs. The uncertainty estimates for the parameters correspond to Gaussian $1-\sigma$ limits which have, in the case of fractions, been computed assuming that a binomial distribution can be approximated by a Gaussian distribution in the limit of large N . Correlations between the variables are not readily available so for error propagation we have assumed that they are uncorrelated.

At this point we stress that there are some important assumptions in our calculation of the TCO SFD:

- The orbit-density distribution is assumed to be independent of the SFD. While this assumption is probably valid for large NEOs it is certainly not true for the meter-class and smaller NEOs for which non-gravitational forces play an important role in the dynamical evolution of their orbits. However, since no debiased NEO orbit distribution exists for the small NEOs we have no option but to make this assumption. On the other hand, we expect that this work will provide constraints on the dynamical evolution of small NEOs and their orbit distribution once techniques are developed for identifying large numbers of TCOs.
- The fraction of NEOs on Earth-like orbits is assumed to be exactly known because uncertainty estimates are not provided with the orbit-density distribution by Bottke et al. (2002). When estimating the inte-

gral in Eq. 8 we also assumed that the capture efficiency as a function of orbital elements is known exactly.

- The measured SFDs for the NEO source population extend to only $H \sim 34$ so our calculation of the TCO SFD to smaller sizes is pure extrapolation.

To calculate the TCO SFD we first need to determine the fractional decay rate, r_{ISP} , for the first flux calculation, F_{TCO1} , (see Sect. 2.5.1). To this end, we calculate the time t it takes for each TCO to get from a geocentric distance of 0.05 AU to the point of capture (i.e. correcting for the fact that the TPs were generated in a shell at geocentric distances from 0.04 to 0.05 AU) and plot the natural logarithm of the number of TPs still remaining to be captured as a function of t (Fig. 16). The fractional decay rate is the slope of this distribution — but the slope is not constant so the measured fractional decay rate will depend on the time interval over which the slope is measured. Instead, we measured the running slope over each 7 day interval and then calculating the number-weighted slope as the weighted average with weights equal to the number of objects in each 7 day interval yielding

$$F_{\text{TCO1}}(H = 24) = (3.78 \pm 1.92) \times 10^{-7} \text{ d}^{-1}.$$

For the second method of calculating the TCO flux we need to know the number of objects in the ISP, N_{ISP} , with $H = 24$, the average lifetime in the ISP, \bar{L}_{ISP} , and the fraction $f_{\text{TCO/ISP}}$ of TPs in the ISP that eventually become TCOs (see Sect. 2.5.2). $N_{\text{ISP}}(H = 24) = N_0 \times R_{\text{ISP}} \times f_{\text{ISP/NEO}} \sim (4.02 \pm 0.54) \times 10^{-3}$ while the average lifetime in the ISP, \bar{L}_{ISP} , and fraction of TPs in the ISP that eventually become TCOs, $f_{\text{TCO/ISP}}$, are obtained directly from the integration results; $(3.991 \pm 0.022) \times 10^1 \text{ d}$ and $(1.810 \pm 0.013) \times 10^{-3}$, respectively. The flux of TCOs using the second method is then

$$F_{\text{TCO2}}(H = 24) = (1.82 \pm 0.25) \times 10^{-7} \text{ d}^{-1}.$$

The agreement between F_{TCO1} and F_{TCO2} is surprisingly good considering that the fractional decay rate needed for F_{TCO1} is computed assuming a constant slope — an assumption that does not hold in this particular case because the slope is variable for any reasonable time interval.

Figure 17 shows that the TCO steady-state SFD depends strongly on the assumed NEO source population’s SFD and only weakly on our method

of calculating the TCO flux. There is approximately 3 orders of magnitude difference in the predicted number of TCOs larger than one meter in diameter ($H \lesssim 32$).

We can use the one confirmed TCO (2006 RH₁₂₀) with a diameter of a few meters to discriminate between the three NEO population models keeping in mind that no knowledge of 2006 RH₁₂₀ was used in our TCO modeling. In the steady state the Rabinowitz et al. (2000), Brown et al. (2002), and Bottke et al. (2000) models predict that the largest TCO always present in the steady-state population is ~ 3 -m, ~ 1 -m and ~ 0.2 -m in diameter, respectively. If there really were one 3-meter diameter in orbit at any time we would expect for many more of these objects to be known. Similarly, the Bottke et al. (2000) model suggests that the time interval between TCOs in 2006 RH₁₂₀'s size range is > 100 years implying that the odds of finding such an object are small. Thus, the NEO SFD model that is most consistent with the observed TCO distribution is the Brown et al. (2002) model.

3.6 Orbit characteristics and residence-time distributions for temporarily-captured orbiters

Figures 18 and 19 illustrate that the TCO's osculating geocentric orbital elements change dramatically on short timescales. A geocentric two-body orbit is not adequate for describing the motion of TCOs even for relatively short time periods.

The residence-time distributions shown in Fig. 20 were created by logging the time that each TCO spends in each bin in the binned phase space and then normalizing the distribution. They can be thought of as the instantaneous probability distributions for the orbital elements of TCO population. The distribution shows that NEOs can be captured and evolve into almost any geocentric orbit although low- a_g -high- e_g orbits are strongly preferred (note that the density scale is logarithmic). This can partly be understood as a direct consequence of the fact that, in the geocentric frame, all TCOs start and end with low- a_g and high- e_g because they are on hyperbolic geocentric orbits prior to capture and after escape. However, since Fig. 21 shows that low- a_g and high- e_g orbits are prominent in the residence-time distributions for TCOs completing more than five revolutions, low- a_g and high- e_g orbits are preferred throughout long capture events. Note also that retrograde orbits are slightly preference over prograde orbits.

The inclination distribution has a spike at ($a_g \sim 0.001$ AU, $i_g \sim 35^\circ$) that is due to only a handful of objects that have lifetimes up to 1000x longer than the average TCO. These very long-lived TCOs evolve through, for example, multiple lunar close approaches, into orbits with apogees within the Moon’s orbit. They are affected by the Kozai resonance (Kozai 1962) as revealed by Kozai synchronous oscillations in e and i (Fig. 22) and the libration of the argument of perigee around $\omega = 270^\circ$ (Fig. 23). These orbital features prevent long-lived TCOs from having close encounters with the Moon on short timescales.

We did not discover any temporary lunar satellites fulfilling the TCO criteria. We did find cases where the lunacentric Kepler energy was negative for a short period of time but those TPs were not captured long enough to complete a full revolution around the Moon.

3.7 Terrestrial and lunar impacts by temporarily-captured orbiters

About 1% — 169 out of 18,096 — of all TCOs in our sample impacted the Earth while being captured. The impact probability increases with the duration of the capture so that about 18% of TCOs with lifetimes longer than 6 years eventually impact the Earth. The opportunity of observing meteors and finding meteorites subsequent to the TCO phase suggests that spectroscopic observations of these bodies will maximize their scientific return (cf. Jenniskens et al. 2009). In an additional 20 other cases (0.1% of all TCOs) a terrestrial impact happened more than one week after the TCO had escaped the EMS but within about one to three years from the generation epoch.

A comparison of the rate of TCO-impactors to the background population of impactors is nontrivial because only slow-moving objects were integrated in the present work and TCOs occupy a smaller volume of the phase space than non-TCOs (Fig. 24). However, a rough comparison can be done if we limit consideration to the slow-moving population and assume that the phase-space-volume differences can be neglected by concentrating on two volumes harboring TCOs. A limited volume of the phase-space is defined as $e_h < 0.035$, $i_h < 1^\circ$ and 0.97 AU $< a_h < 0.995$ AU or 1.005 AU $< a_h < 1.03$ AU. This limited volume contains 575,100 TPs to be integrated and out of those 14,909 become TCOs. Terrestrial impacts occur for 1,114 TPs and 104 of those were TCOs. The TCO impact rate in the constrained phase

space is thus $104/14909 \approx 0.7\%$ whereas the fraction of non-TCOs on similar generated orbits producing impacts is $(1114 - 104)/(575100 - 14909) \approx 0.2\%$. In other words, TCOs are nominally 3.5x more likely to impact the Earth than non-TCOs on initially similar heliocentric orbits.

The fraction of all Earth-impacting objects that were TCOs is surprisingly high. In our integrations 189 TCOs impact the Earth during a time span of 19 years so the annual TCO Earth-impact rate from TCOs is about 10 yr^{-1} . (Note that the following reasoning does not depend on the time span nor the number of TPs.) To determine the diameter of objects corresponding to this impact rate we note that the average annual unnormalized (that is, raw) number of TCOs is about 952 yr^{-1} which means that the corresponding unnormalized steady-state population is about 707 TCOs (after multiplying by the average TCO lifetime). Figure 17 shows that the normalized steady-state population corresponding to this number of objects have a maximum absolute magnitude of $H \sim 37$ or a minimum diameter of about 10 cm. Thus, the sizes of the above-mentioned annual TCO impactors are typically 10 cm because the size distribution for the impactors must be heavily skewed towards the smallest sizes. Since Brown et al. (2002) states that there are about 10^4 objects larger than 10 cm impacting the Earth every year, about 0.1% of all Earth impactors are TCOs.

The terrestrial impact-speed distribution is extremely narrow with a peak at approximately the Earth's escape speed, 11.2 km s^{-1} (Fig. 25). Indeed, Fig. 26 shows that the TCO speed distribution as a function of geocentric distance is essentially that of objects falling towards the Earth after starting with almost zero speed. The impact-angle¹ distribution shows that TCO impacts span essentially the whole range of possible angles (Fig. 27). Recall, however, that the present work does not take into account non-gravitational effects such as atmospheric drag which could change the distribution of impact angles. These predictions may provide a means to differentiate between TCOs and other meteors in radar data although it is unclear to us whether the signal from NESs is strong enough to overcome the background flux from, e.g., other meteor populations or spacecraft debris re-entering the atmosphere. The detection of slow-moving meteors is also massively biased against. There are, however, recorded meteors with apparent speeds less than Earth's escape speed but it is not clear whether these objects are natural or whether the

¹The acute angle between the trajectory and the perpendicular to the Earth's 'surface' (nearly equivalent to the atmospheric impact 'surface') at the point of impact.

low speeds are due to deceleration before detection (personal communication with P. Brown). We will discuss various techniques for discovering TCOs in a forthcoming paper on their observational characteristics.

None of the TCOs impacted the moon so this class of events is extremely rare. In fact, only one lunar impact occurred during the integrations of 10^7 TPs suggesting that low-speed lunar impacts in general are extremely rare.

3.8 Heliocentric orbit characteristics after a temporary capture

The TCOs escape the EMS using the same route as during the capture — through the L1 and L2 points. This is a direct consequence of the time reversibility of the gravitational-capture event. We integrated each TCO (that did not impact the Earth) 1 yr forward in time from the last date that it had $e_g < 1$ to find out how its post-capture orbit compared to its pre-capture orbit. We checked that most TPs are sufficiently far from the Earth at this stage so that perturbations by the Earth on their orbits can be neglected. The major difference between heliocentric pre-capture and post-capture orbits for TCOs is the widening of the gap at $a_h \sim 1$ AU (Fig. 28). Although this would seem to indicate that it is essentially only the semimajor axes that get pushed away from the $a_h \sim 1$ AU line, the reality is a bit more complex. Figure 29 shows that some TPs that were TCOs entered the EMS on orbits with $a_h > 1$ AU and leave on orbits with $a_h < 1$ AU, and vice versa. There is also a clear zone of avoidance so that orbits with $a_h \sim 1$ AU are dynamically impossible to reach. The fractional changes in eccentricity and inclination can be large and behave much like the semimajor axes but without the ‘zone of avoidance’ — that is, large eccentricities and/or inclinations tend to get smaller and small eccentricities and/or inclinations tend to get larger.

The fact that the volume and shape of the post-capture orbit distributions matches the volume and shape of the pre-capture distributions can, again, be understood as a direct consequence of the time reversibility of gravitational-capture events. The similarity of the distributions suggests that a single object may be captured on several different occasions before planetary perturbations force it to leave the volume harboring capturable orbits.

4 Conclusions

We provide the first estimate of the orbit and size-distribution for temporarily captured natural irregular satellites of the Earth. We predict that there is a one-meter-diameter or larger NEO temporarily orbiting the Earth at any given time. The NEO orbit and SFD model is currently the main factor limiting the accuracy of our predictions. Given the orbit distribution of Bottke et al. (2002) the Brown et al. (2002) NEO SFD is consistent with the only known TCO of natural origin, 2006 RH₁₂₀, while the Bottke et al. (2002) and Rabinowitz et al. (2000) SFDs are each off by about an order of magnitude.

Our integrated TCO population will allow us to examine different scenarios for their detection and to estimate, e.g., the average time from discovery to an accurately known orbit. It seems plausible that the long-lived TCOs could have stable enough orbits to allow successful searches to be carried out in specific regions of the sky. Once TCOs can be reliably and frequently identified early enough in a capture event they create an opportunity for a low-cost low-delta-v meteoroid return mission (cf. Elvis et al. 2011). The scientific potential of being able to first remotely characterize a meteoroid and then visit and bring it back to Earth would be unprecedented.

Acknowledgments

We acknowledge the thorough reviews by A. Christou and an anonymous reviewer as well as helpful discussions with B. Gladman and P. Wiegert concerning TCO dynamics, P. Chodas and L. Benner concerning 2006 RH₁₂₀, and P. Brown concerning detection of NES meteors. MG's and RJ's work was funded by a grant from the NASA NEOO program (NNX07AL28G). MG was also funded by grants #130989, #136132 and #137853 from the Academy of Finland. JV thanks the CINES team for the use of the Jade SGI supercluster and their help in parallelizing the orbital integration code.

References

- Bagby, J. P. (1969), ‘Terrestrial Satellites: Some Direct and Indirect Evidence’, *Icarus* **10**, 1–10.
- Baker, Jr., R. M. L. (1958), ‘Ephemeral Natural Satellites of the Earth’, *Science* **128**, 1211–1213.
- Baoyin, H.-X., Chen, Y. & Li, J.-F. (2010), ‘Capturing Near Earth Objects’, *Research in Astronomy and Astrophysics* **10**, 587–598.
- Bottke, W. F., Jedicke, R., Morbidelli, A., Petit, J.-M. & Gladman, B. (2000), ‘Understanding the Distribution of Near-Earth Asteroids’, *Science* **288**, 2190–2194.
- Bottke, W. F., Morbidelli, A., Jedicke, R., Petit, J. M., Levison, H. F., Michel, P. & Metcalfe, T. S. (2002), ‘Debiased Orbital and Absolute Magnitude Distribution of the Near-Earth Objects’, *Icarus* **156**(2), 399–433.
- Brasser, R. & Wiegert, P. (2008), ‘Asteroids on Earth-like orbits and their origin’, *MNRAS* **386**, 2031–2038.
- Brown, P., Spalding, R. E., ReVelle, D. O., Tagliaferri, E. & Worden, S. P. (2002), ‘The flux of small near-Earth objects colliding with the Earth’, *Nature* **420**, 294–296.
- Carusi, A. & Valsecchi, G. B. (1979), Numerical simulations of close encounters between Jupiter and minor bodies, *in* Gehrels, T., ed., ‘Asteroids’, pp. 391–416.
- Cassidy, W. A., Villar, L. M., Bunch, T. E., Kohman, T. P. & Milton, D. J. (1965), ‘Meteorites and Craters of Campo del Cielo, Argentina’, *Science* **149**, 1055–1064.
- Chant, C. A. (1913), ‘An Extraordinary Meteoric Display’, *JRASC* **7**, 144–215.
- Cline, J. K. (1979), ‘Satellite aided capture’, *Celestial Mechanics* **19**, 405–415.

- Denning, W. F. (1916), ‘The Remarkable Meteors of February 9, 1913’, *Nature* **97**, 181.
- Elvis, M., McDowell, J., Hoffman, J. A. & Binzel, R. P. (2011), ‘Ultra-low delta-v objects and the human exploration of asteroids’, *Planetary and Space Science* **59**(13), 1408–1412.
- Fienga, A., Manche, H., Laskar, J. & Gastineau, M. (2008), ‘INPOP06: a new numerical planetary ephemeris’, *A&A* **477**, 315–327.
- Iwasaki, K. & Ohtsuki, K. (2007), ‘Dynamical behaviour of planetesimals temporarily captured by a planet from heliocentric orbits: basic formulation and the case of low random velocity’, *MNRAS* **377**, 1763–1771.
- Jedicke, R. (1996), ‘Detection of near earth asteroids based upon their rates of motion’, *Astron. J.* **111**(2), 970–982.
- Jedicke, R., Larsen, J. & Spahr, T. (2002), Observational Selection Effects in Asteroid Surveys and Estimates of Asteroid Population Sizes, *in* W. Bottke, A. Cellino, P. Paolicchi & R. P. Binzel, eds, ‘Asteroids III’, University of Arizona Press, pp. 71–87.
- Jenniskens, P., Shaddad, M. H., Numan, D., Elsir, S., Kudoda, A. M., Zolensky, M. E., Le, L., Robinson, G. A., Friedrich, J. M., Rumble, D., Steele, A., Chesley, S. R., Fitzsimmons, A., Duddy, S., Hsieh, H. H., Ramsay, G., Brown, P. G., Edwards, W. N., Tagliaferri, E., Boslough, M. B., Spalding, R. E., Dantowitz, R., Kozubal, M., Pravec, P., Borovicka, J., Charvat, Z., Vaubaillon, J., Kuiper, J., Albers, J., Bishop, J. L., Mancinelli, R. L., Sandford, S. A., Milam, S. N., Nuevo, M. & Worden, S. P. (2009), ‘The impact and recovery of asteroid 2008 TC₃’, *Nature* **458**, 485–488.
- Kary, D. M. & Dones, L. (1996), ‘Capture Statistics of Short-Period Comets: Implications for Comet D/Shoemaker-Levy 9’, *Icarus* **121**, 207–224.
- Kozai, Y. (1962), ‘Secular perturbations of asteroids with high inclination and eccentricity’, *AJ* **67**, 591–598.
- Kwiatkowski, T., Kryszczyńska, A., Polińska, M., Buckley, D. A. H., O’Donoghue, D., Charles, P. A., Crause, L., Crawford, S., Hashimoto, Y., Kniazev, A., Loaring, N., Romero Colmenero, E., Sefako, R., Still,

- M. & Vaisanen, P. (2009), ‘Photometry of 2006 RH₁₂₀: an asteroid temporary captured into a geocentric orbit’, *A&A* **495**, 967–974.
- Meeus, J. (1973), ‘Bagby’s Phantom Moonlets’, *Icarus* **19**, 547–549.
- Mikkola, S., Innanen, K., Wiegert, P., Connors, M. & Brassier, R. (2006), ‘Stability limits for the quasi-satellite orbit’, *MNRAS* **369**, 15–24.
- Morais, M. H. M. & Morbidelli, A. (2002), ‘The Population of Near-Earth Asteroids in Coorbital Motion with the Earth’, *Icarus* **160**, 1–9.
- Murison, M. A. (1989), ‘The fractal dynamics of satellite capture in the circular restricted three-body problem’, *AJ* **98**, 2346–2359.
- Murray, C. D. & Dermott, S. F. (1999), *Solar System Dynamics*, Cambridge University Press, Cambridge, UK.
- O’Keefe, J. A. (1961), ‘Tektites as Natural Earth Satellites’, *Science* **133**, 562–566.
- Rabinowitz, D., Helin, E., Lawrence, K. & Pravdo, S. (2000), ‘A reduced estimate of the number of kilometre-sized near-Earth asteroids’, *Nature* **403**, 165–166.
- Stoer, J. & Bulirsch, R. (2002), *Introduction to Numerical Analysis*, 3 edn, Springer Verlag, New York.
- Tancredi, G. (1997), ‘An Asteroid in a Earth-like Orbit’, *Celestial Mechanics and Dynamical Astronomy* **69**, 119–132.
- Tancredi, G., Lindgren, M. & Rickman, H. (1990), ‘Temporary satellite capture and orbital evolution of Comet P/Helin-Roman-Crockett’, *A&A* **239**, 375–380.
- Werner, S. C., Harris, A. W., Neukum, G. & Ivanov, B. A. (2002), ‘NOTE: The Near-Earth Asteroid Size-Frequency Distribution: A Snapshot of the Lunar Impactor Size-Frequency Distribution’, *Icarus* **156**, 287–290.

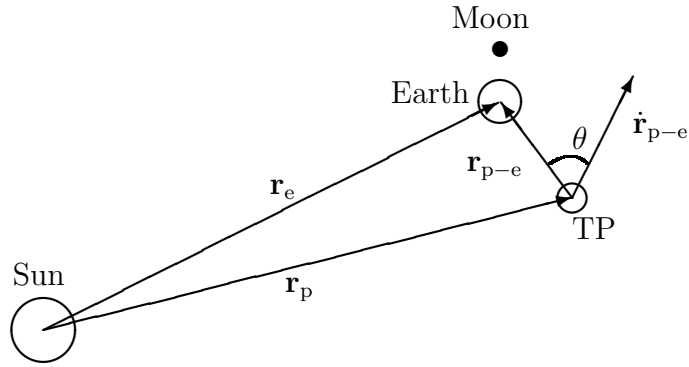


Figure 1: Vector and angle definitions in the Earth-Moon-Sun-object system (not to scale). The test particle's heliocentric position vector and geocentric velocity vector are represented by \mathbf{r}_p and $\dot{\mathbf{r}}_p$, respectively. The Earth's heliocentric position vector is marked with \mathbf{r}_e . The direction angle θ is the angle between the test particle's geocentric velocity and geocentric direction vectors.

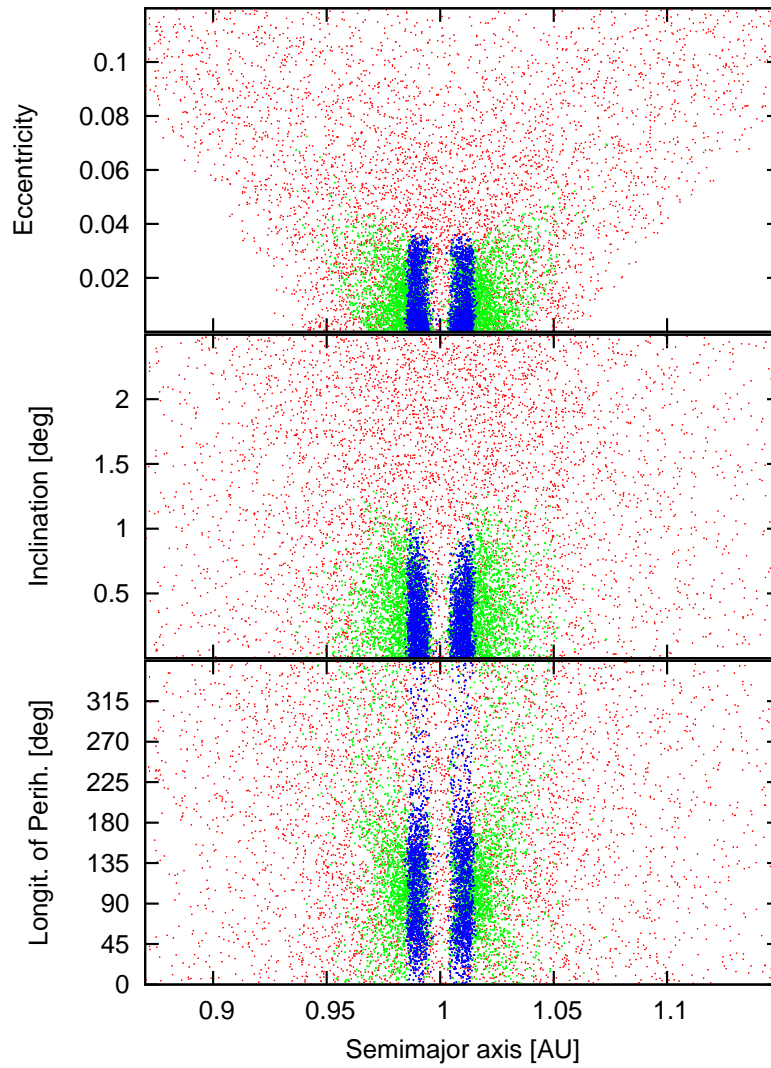


Figure 2: Representative samples of generated heliocentric Keplerian orbital elements for (red) all integrated test particles and temporarily-captured orbiters where the color indicates different intervals for the direction angle at the generation epoch: (green) $0^\circ < \theta_{\text{init}} < 90^\circ$ and (blue) $90^\circ < \theta_{\text{init}} < 120^\circ$.

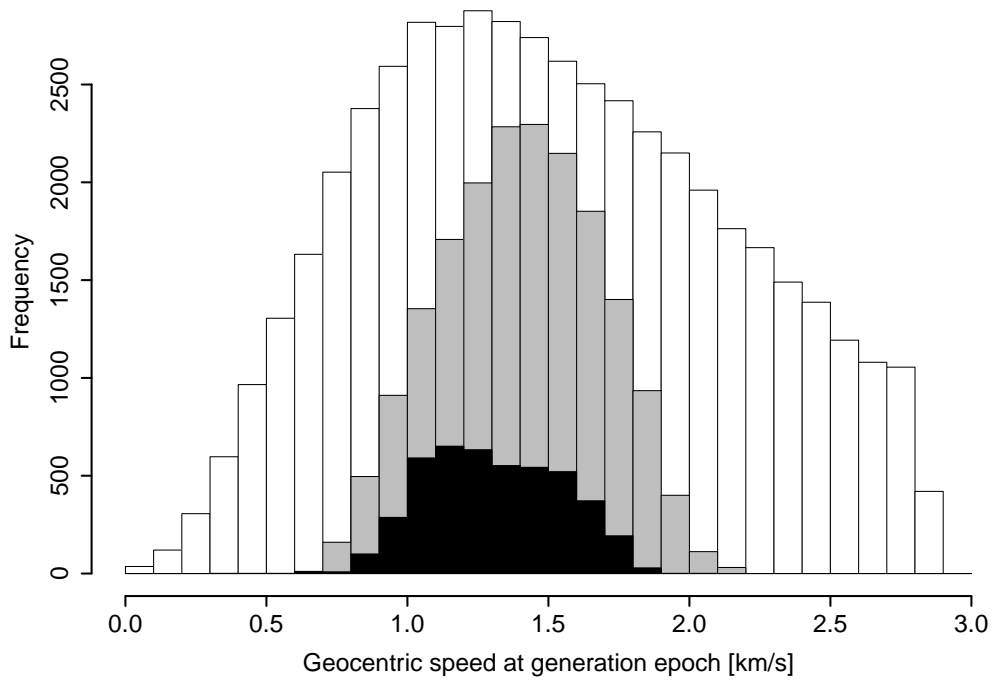


Figure 3: The geocentric speed distribution at the generation epoch for (white) 1/200th of all integrated test particles, (grey) temporarily-captured orbiters in the nominal model and (black) the barycentric model. Note that the mode of the distribution is smaller for the barycentric model.

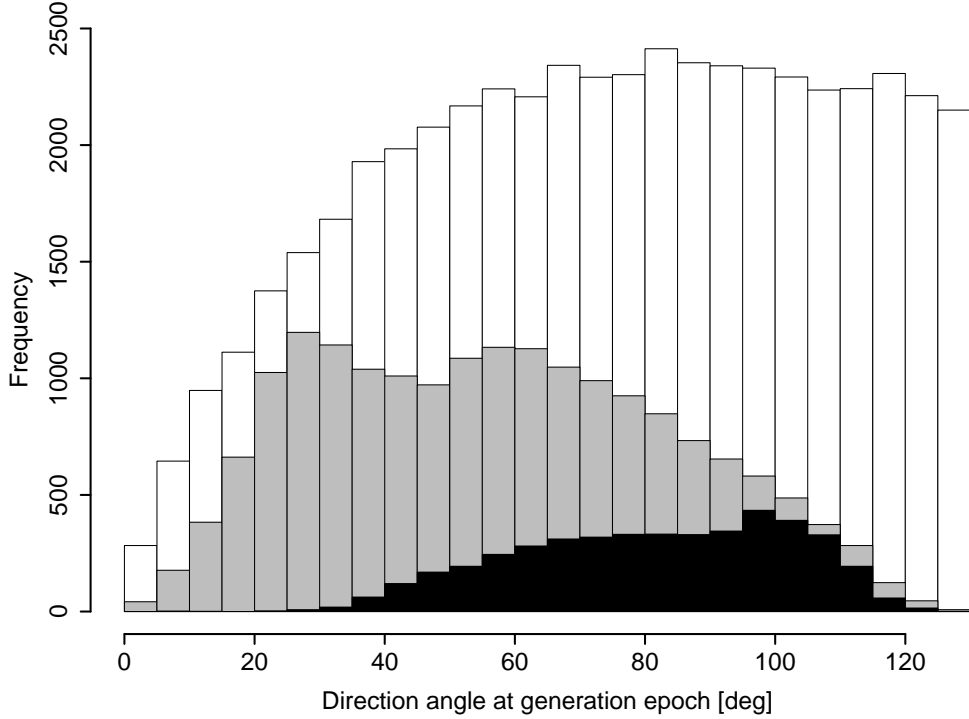


Figure 4: The distribution of direction angles at the generation epoch (θ_{init}) for the three groups of test particles in Fig. 3. At the initial epoch, at geocentric distances between 4 and 5 Hill radii, the TCO direction angles span a wide range of directions. Note that there are TPs that initially move away from the Earth ($\theta_{\text{init}} > 90^\circ$) but are later captured. These objects typically have semimajor axis ~ 1 (Fig. 2) and are not energetically bound to the EMS when they ‘turn around’. TCOs in the barycentric model are more likely to move perpendicular to the Earth than to approach it directly.

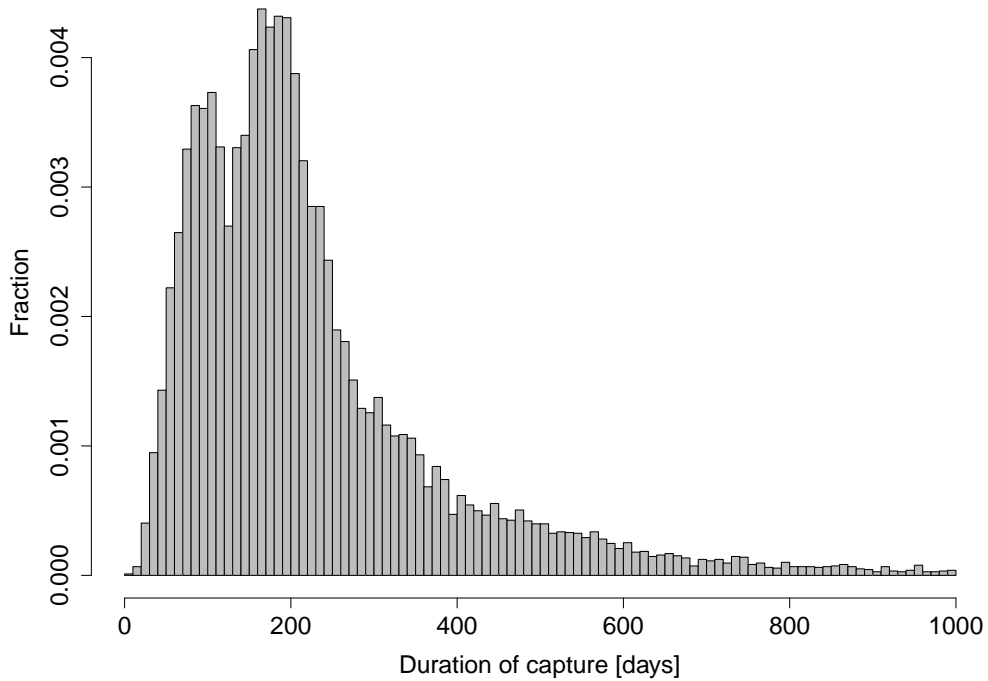


Figure 5: Duration of capture for temporarily-captured orbiters. The longest capture during the integrations lasted about 325,000 days but the histogram has been cut off at 1,000 days. The peaks are located at about 90 days and about 180 days.

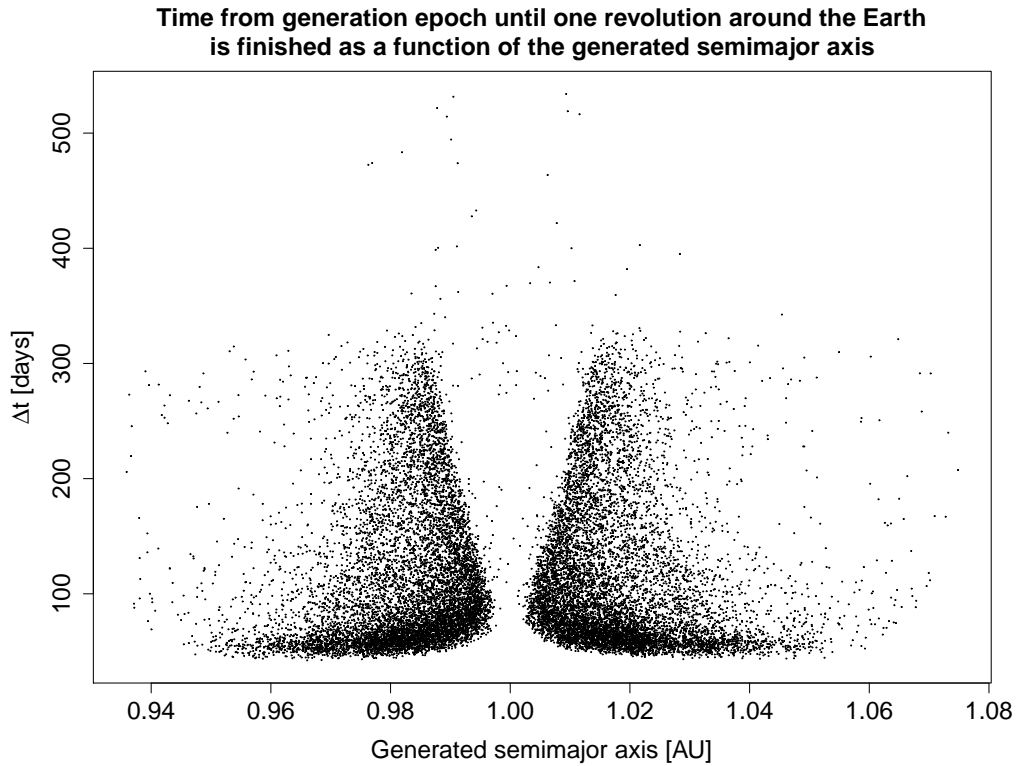


Figure 6: The time it takes for a TP to fulfill the temporarily-captured orbiter criteria starting from the generation epoch. Most temporarily-captured orbiters are detected if the TPs are integrated for more than approximately 500 days. We integrated all the TPs for at least 2,000 days.

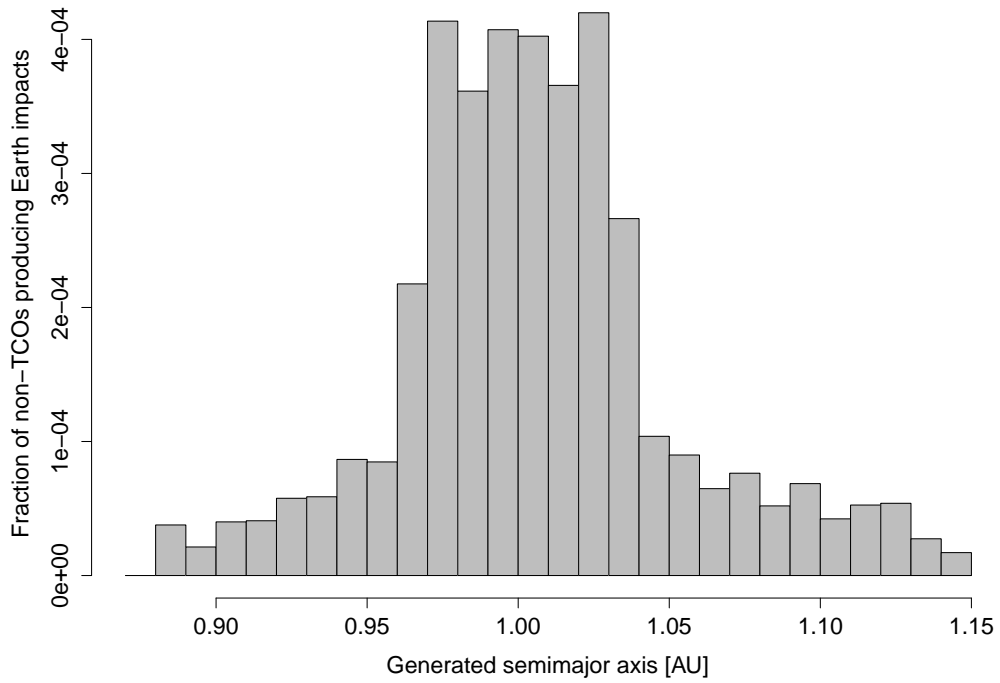


Figure 7: The fraction of TPs colliding with the Earth during a 2,000 day integration as a function of a_h .

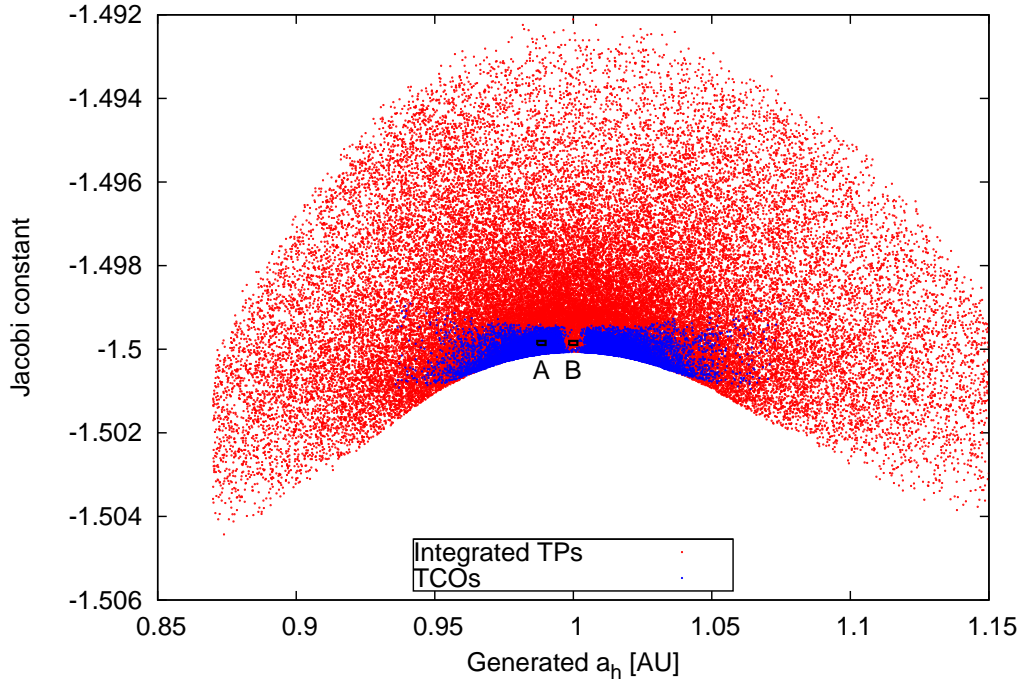


Figure 8: The Jacobi constant, C , as a function of a_h for representative samples of (red) the integrated TPs and (blue) the temporarily-captured orbiters. The black frames labeled 'A' and 'B' mark the regions where two random sets of 100 TPs were chosen to show that the lack of TCOs with $a_h \sim 1$ AU is related to three-body dynamics (see first paragraph in Sect. 3.3 for details). Note that the lack of TCOs in 'B' cannot be explained by too-small Jacobi constants that would prevent TPs from becoming TCOs in that region because the range in C is identical in both regions.

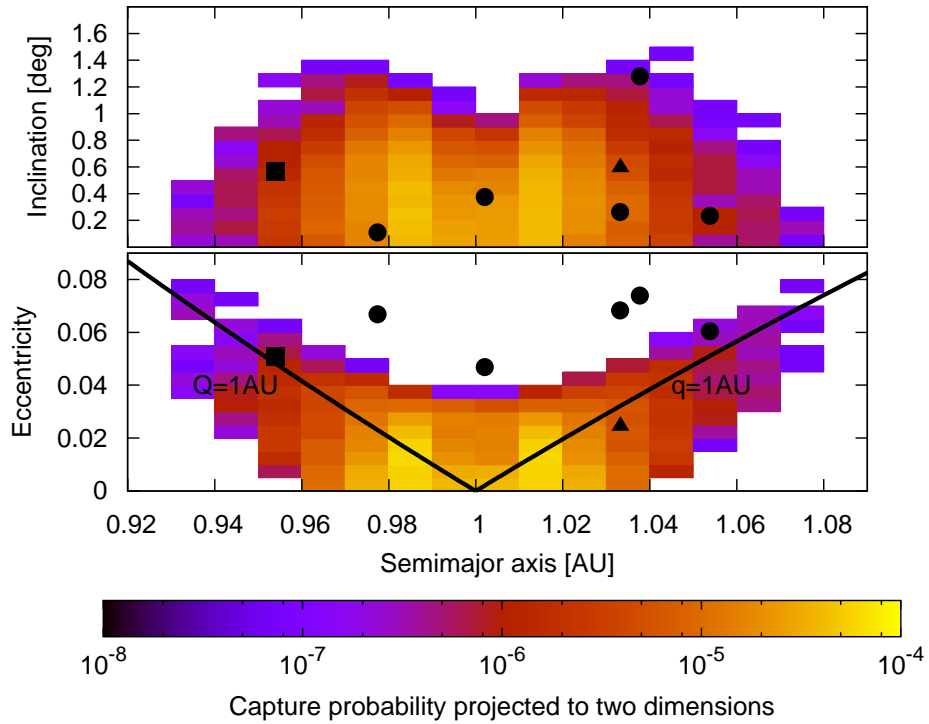


Figure 9: The capture probability in heliocentric (a_h, e_h, i_h) space for temporarily-captured orbiters (TCOs). The wings of the (a_h, e_h) distribution follow the $q = 1$ AU and $Q = 1$ AU lines indicating that a TP on an orbit allowing a grazing encounter with the Earth's orbit may lead to the TP becoming a TCO whereas Earth-crossing orbits in general are not necessarily capturable even with small eccentricities. The pre-capture and current (post-capture) orbital elements for 2006 RH₁₂₀ are indicated with a black square and black triangle, respectively. The current orbital elements for other known NEOs are represented by black circles. The rightmost object in the capturable region is 2007 UN₁₂.

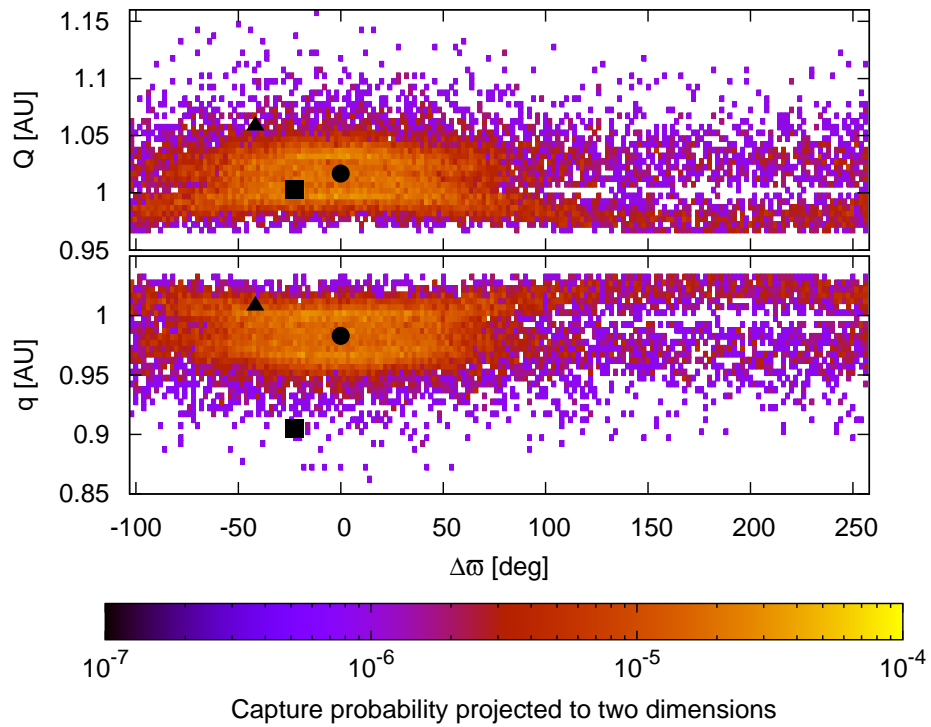


Figure 10: The capture probability in heliocentric $(q_h, Q_h, \varpi_h - \varpi_\oplus)$ space for temporarily-captured orbiters (TCOs). The pre-capture and current (post-capture) orbital elements for 2006 RH₁₂₀ are indicated with a black square and black triangle, respectively. The Earth's orbital elements are marked with a filled black circle.

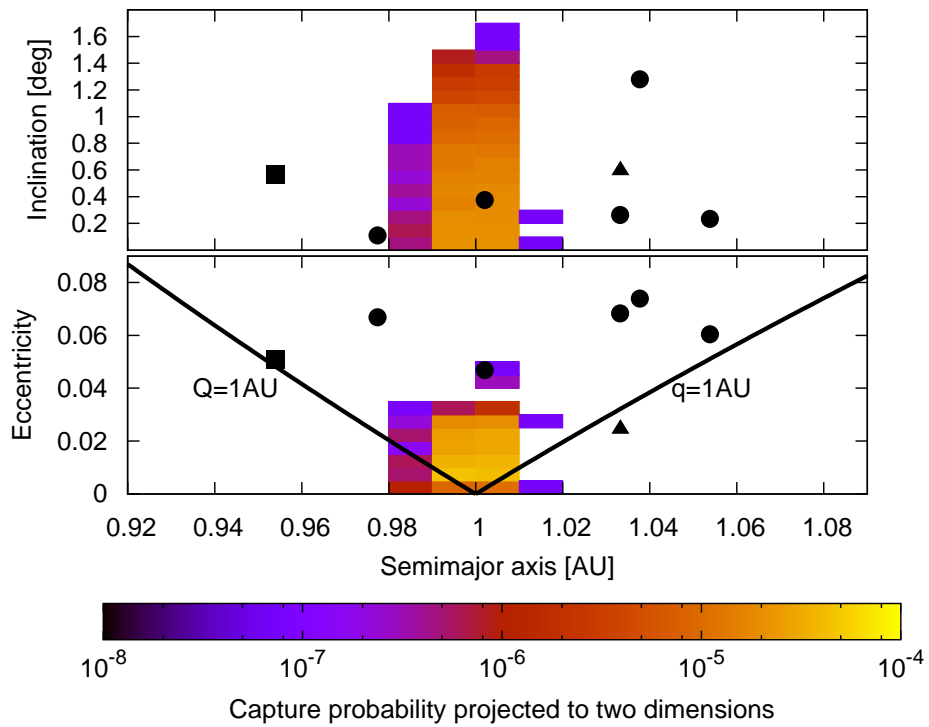


Figure 11: Same as Fig. 9 but for the barycentric dynamical model that does not include the Moon. We note that both the pre-capture orbit and the current (post-capture) orbit for 2006 RH₁₂₀ are outside of the region harboring capturable orbits.

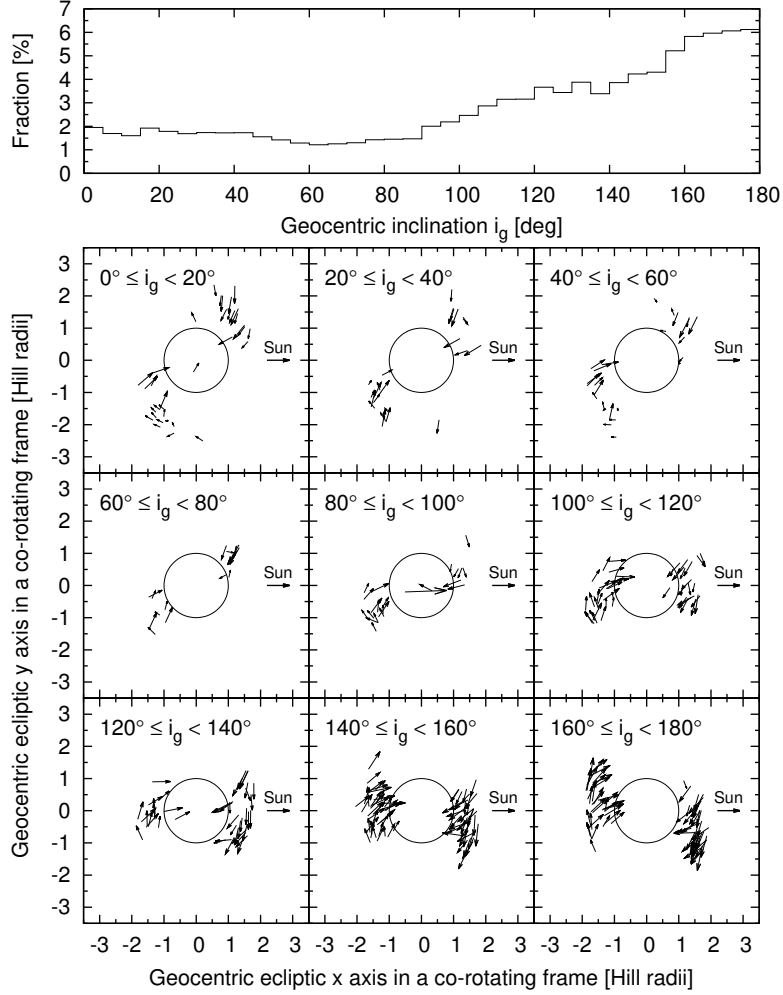


Figure 12: (Top) Fractional distribution of the TCO geocentric inclination distribution. Most TCOs are in retrograde orbits typical of irregular satellites. (Bottom) Positions and instantaneous velocity vectors of temporarily-captured orbiters at time of capture projected onto the ecliptic plane in a co-rotating coordinate system as a function of inclination. For correct interpretation, note that both the prograde ($i_g < 90^\circ$) and retrograde ($i_g > 90^\circ$) TCOs typically move in a retrograde fashion in the co-rotating system: the prograde ones with an average angular rate of $-0.43^\circ \text{ d}^{-1}$ and the retrograde ones with an average angular rate of $-1.6^\circ \text{ d}^{-1}$.

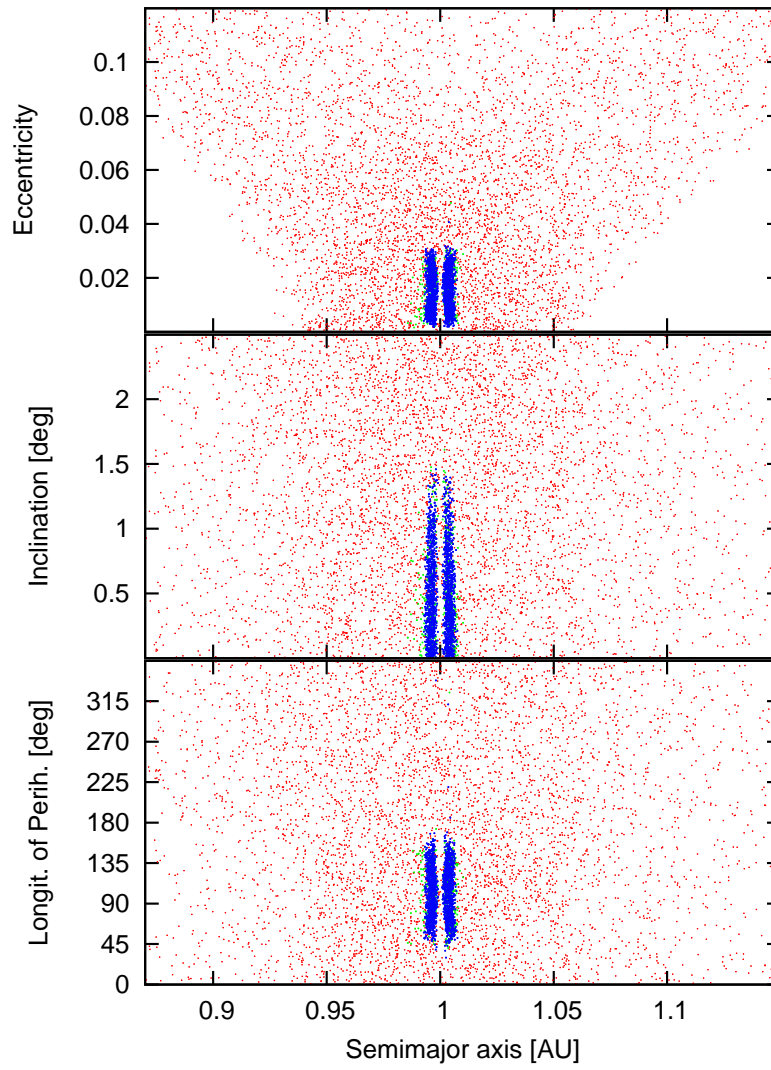


Figure 13: The same as Fig. 2 but for the barycentric model where the Moon has been omitted.

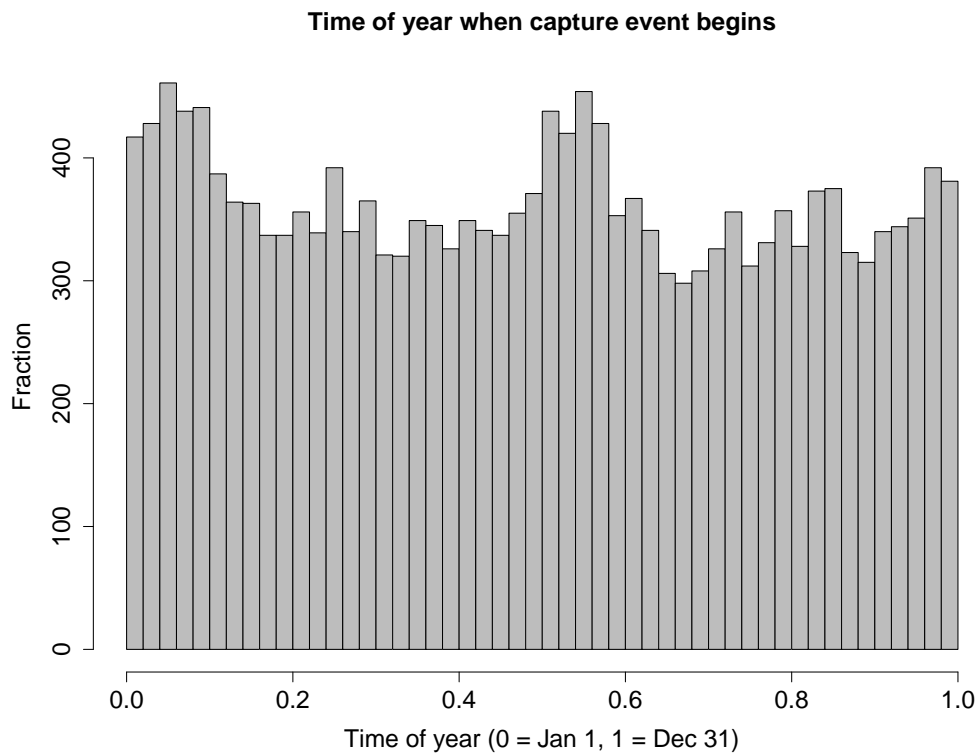


Figure 14: The time of year a temporarily-captured orbiter is captured. The distribution of generation epochs was uniform but the time-of-capture distribution has maxima in January and July.

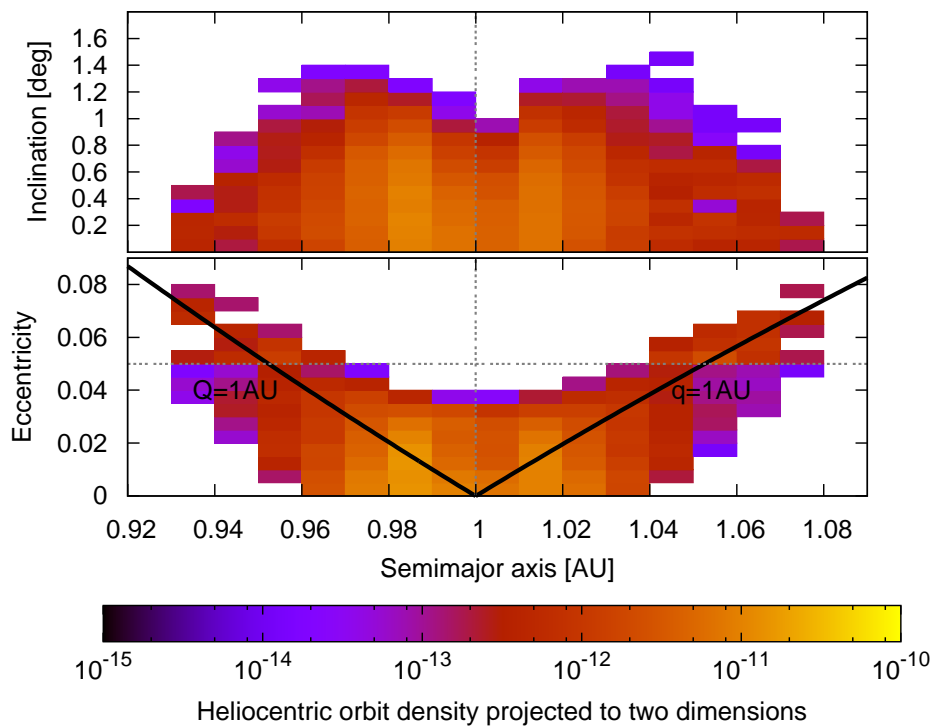


Figure 15: The heliocentric orbit-density distribution for TCOs at the generation epoch, i.e., the product of the capture-probability distribution (see Fig. 9) and the debiased NEO orbit-density distribution (Bottke et al. 2002). The dotted gray lines indicate the resolution of the NEO orbit-density distribution.

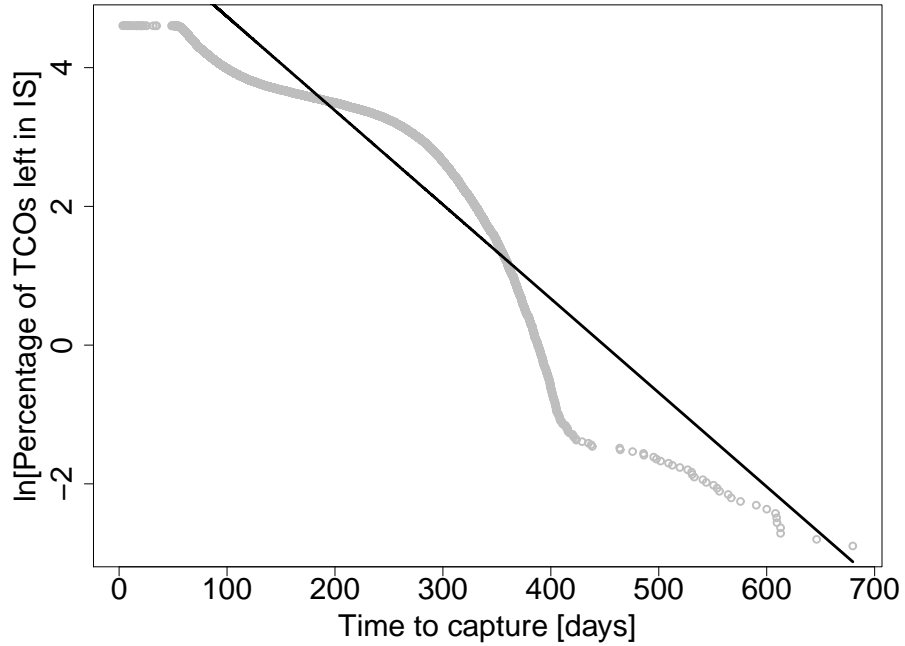


Figure 16: Decay from the outer edge of the intermediate source population (the generated NEOs propagated out to 5 Earth Hill radii from the Earth) into the temporarily-captured orbiter population. The black line represents a number-weighted fit for the slope (see Sect. 3.5 for details). Note that most of the weight is approximately in the interval from 55 to 85 days.

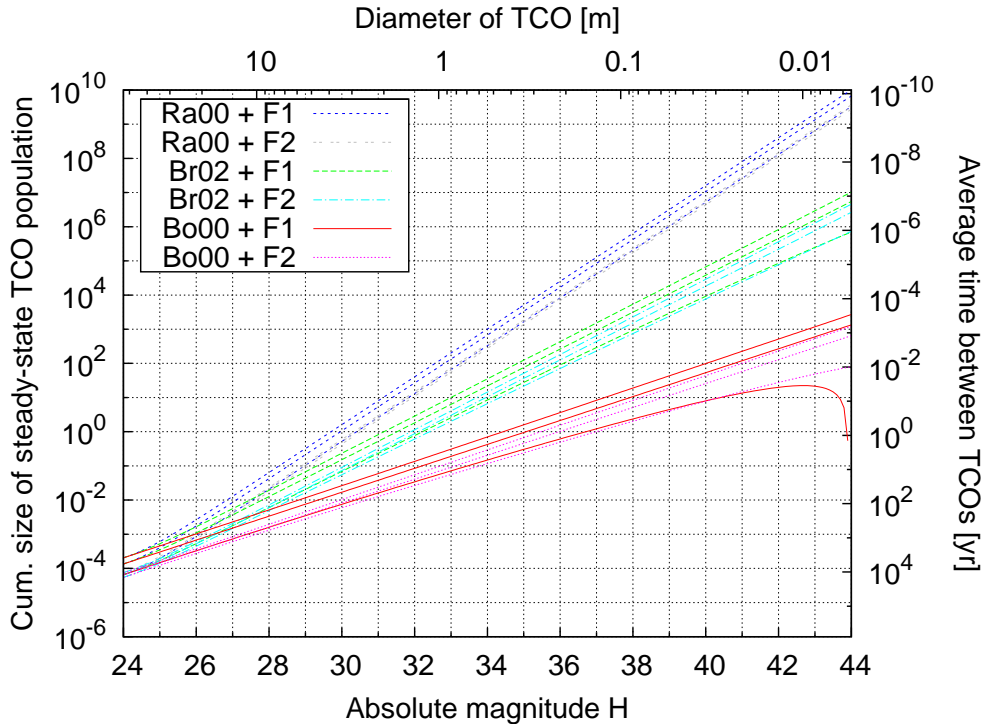


Figure 17: The cumulative steady-state SFD, $N(< H)$, for temporarily-captured orbiters using three different NEO SFDs and two different methods of calculating F_{TCO} (F1 refers to the method used by Morais & Morbidelli (2002) and F2 to the alternative method presented in this work). In the text we argue that F2 and the Brown et al. (2002) NEO SFD provide the most robust estimate which means that the maximum size at which at least one object is captured at any given time is $H \sim 32$ (or a diameter of approximately 1 m), and that the frequency of temporarily-captured orbiters with $H \sim 30$ is about one every decade. The uncertainty envelopes correspond to the $1-\sigma$ uncertainties for the size of the steady-state population that incorporate uncertainty estimates for all other factors but the NEO orbit distribution by Bottke et al. (2002), the capture-efficiency distribution, and the slope for the NEO SFD by Rabinowitz et al. (2000). Note that the envelopes can thus not be directly used to estimate the uncertainty of the frequency of temporarily-captured orbiters on the RHS axis. The conversion from H magnitude to diameter assumes a geometric albedo of 0.15.

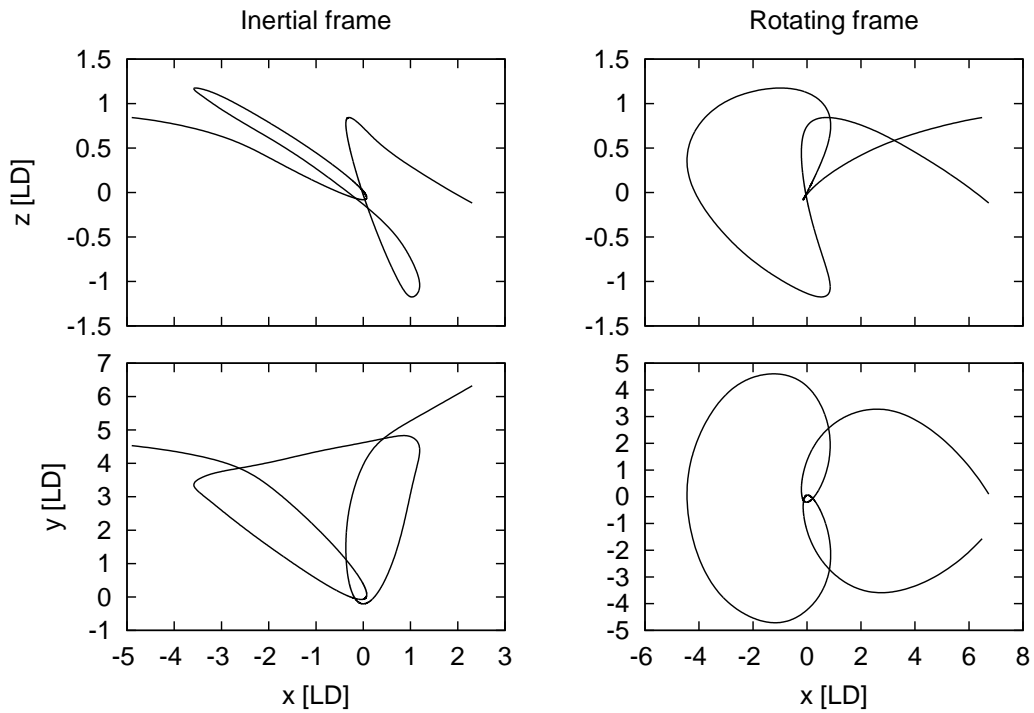


Figure 18: The trajectory of a temporarily-captured orbiter in (left column) geocentric, inertial Cartesian coordinates and (right column) geocentric, co-rotating Cartesian coordinates. This particular TP was chosen because of its close-to-average characteristics: during its 280-day capture it makes 2.94 retrograde revolutions around the Earth as measured in a co-rotating frame. The distance scale is given in lunar distances (LD) equaling approximately 0.00257 AU.

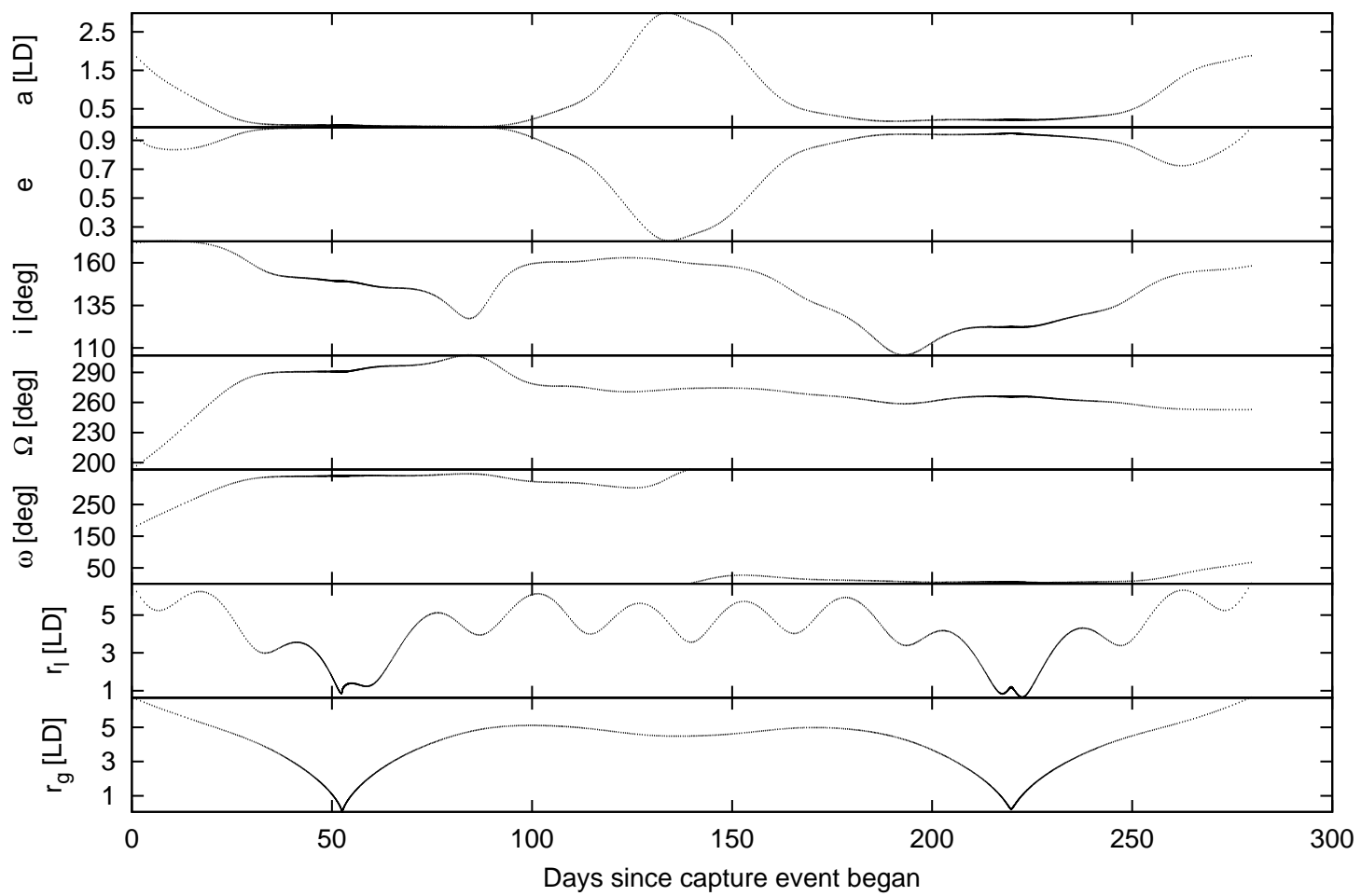


Figure 19: The evolution of the geocentric Keplerian elements and the lunar and geocentric distances for the same object as in Fig. 18. The distance scale is in lunar distances (LD) equaling ~ 0.00257 AU.

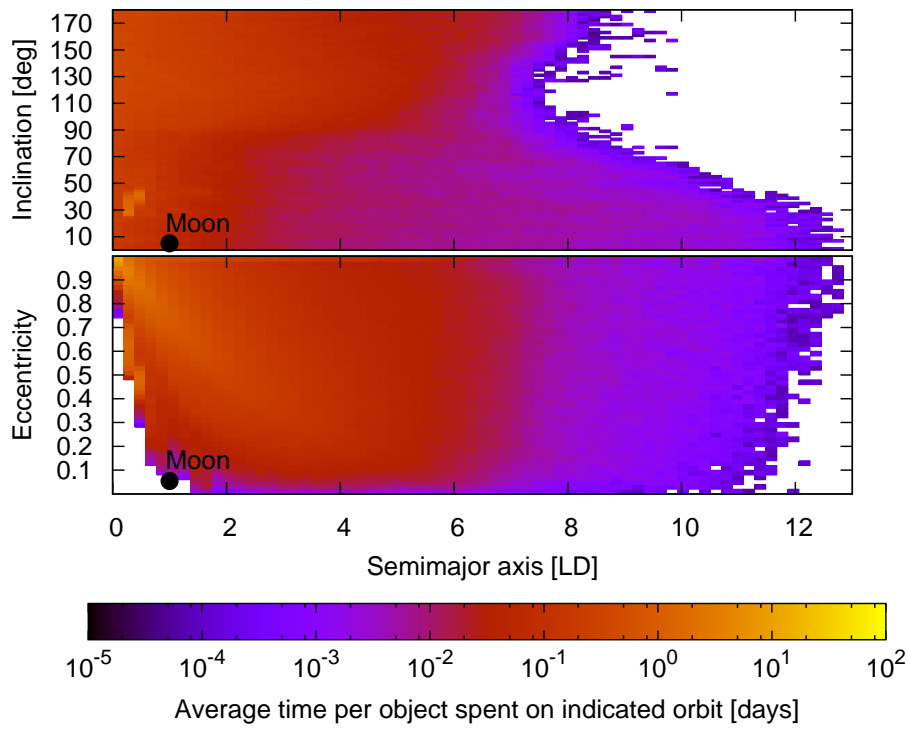


Figure 20: The residence time as a function of geocentric (a_g, e_g, i_g) for temporarily-captured orbiters.

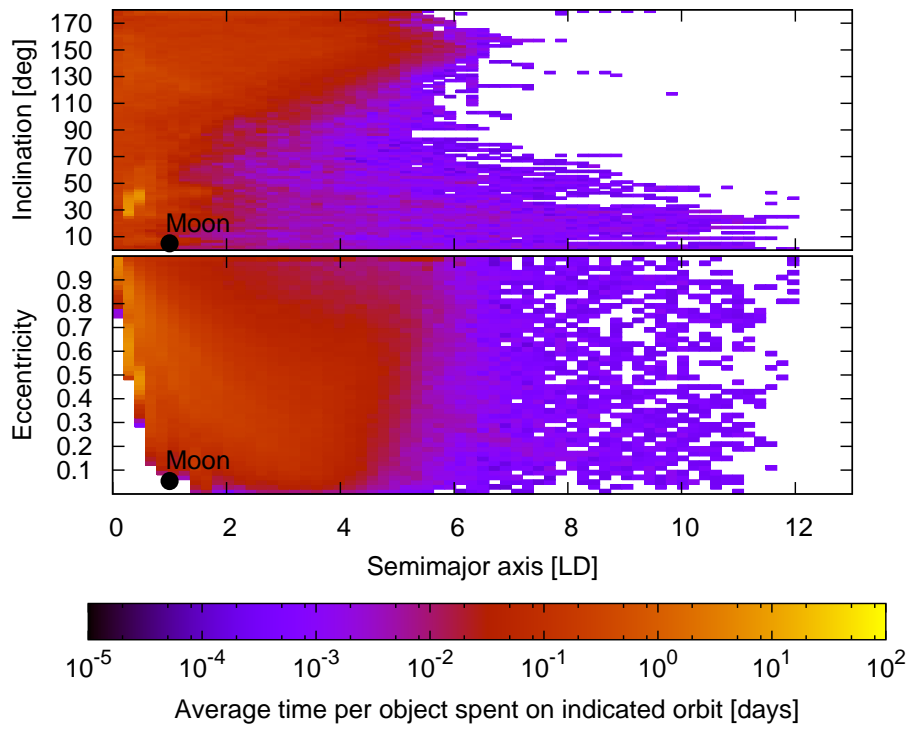


Figure 21: The residence time as a function of geocentric (a_g, e_g, i_g) for the subset of temporarily-captured orbiters that make at least five revolutions around the Earth.

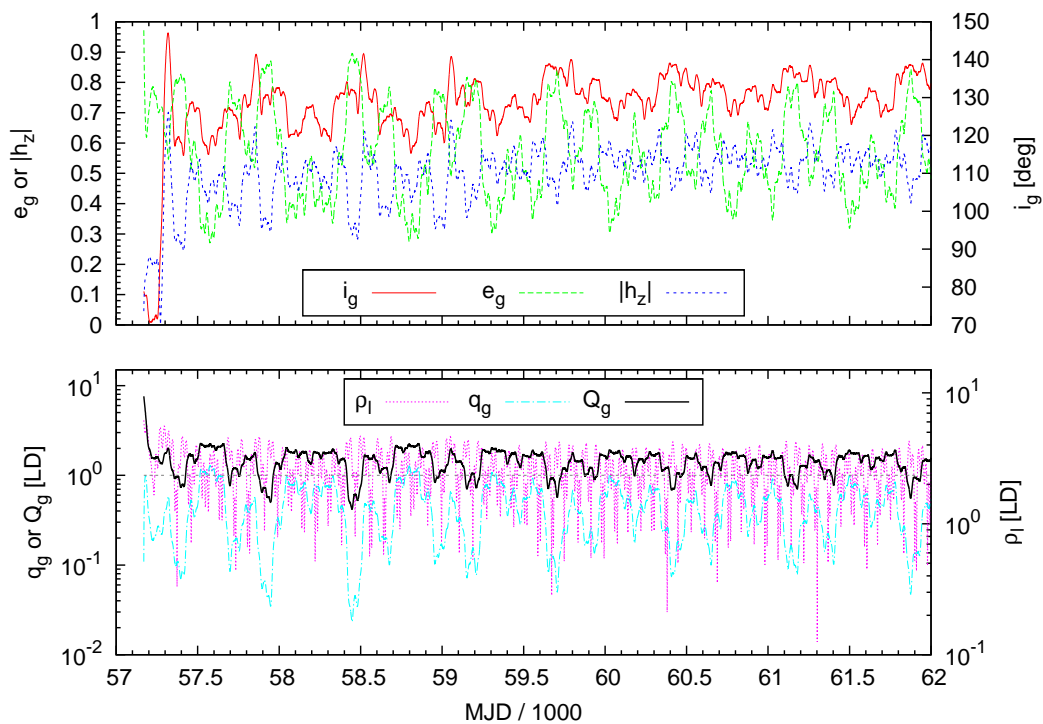


Figure 22: Geocentric orbital-element evolution for a temporarily-captured orbiter that is strongly affected by the Kozai resonance (inclination i_g , eccentricity e_g , the normal component of the angular momentum $|h_z|$, lunacentric distance ρ_l , perigee q_g , and the apogee Q_g). The figure represents the first 13 years of a 35-year-long capture. The horizontal dashed line in the bottom figure represents one lunar distance.

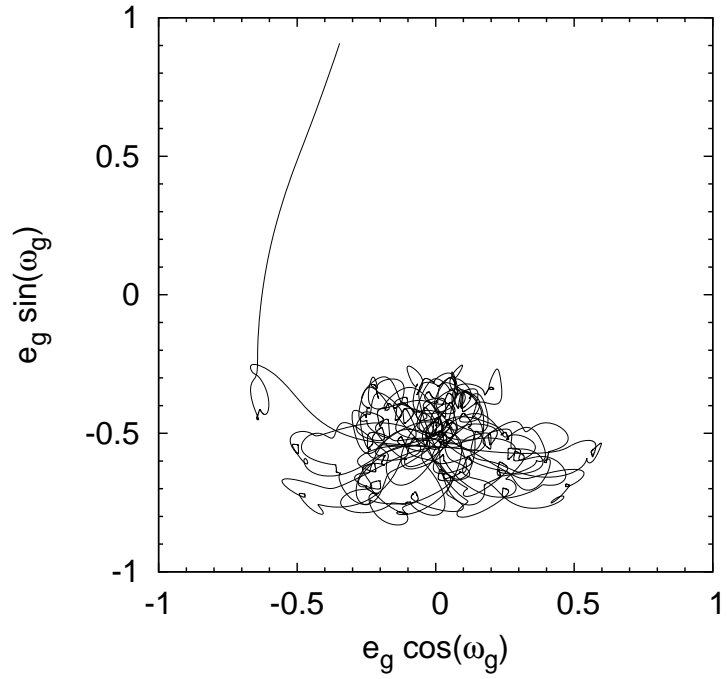


Figure 23: The polar plot for the object in Fig. 22. The geocentric orbit is strongly perturbed by the Sun. The argument of pericenter is librating around $\omega_g = 270^\circ$ which, combined with the e_g-i_g oscillation shown in Fig. 22, reveals that this TP is strongly affected by the Kozai resonance.

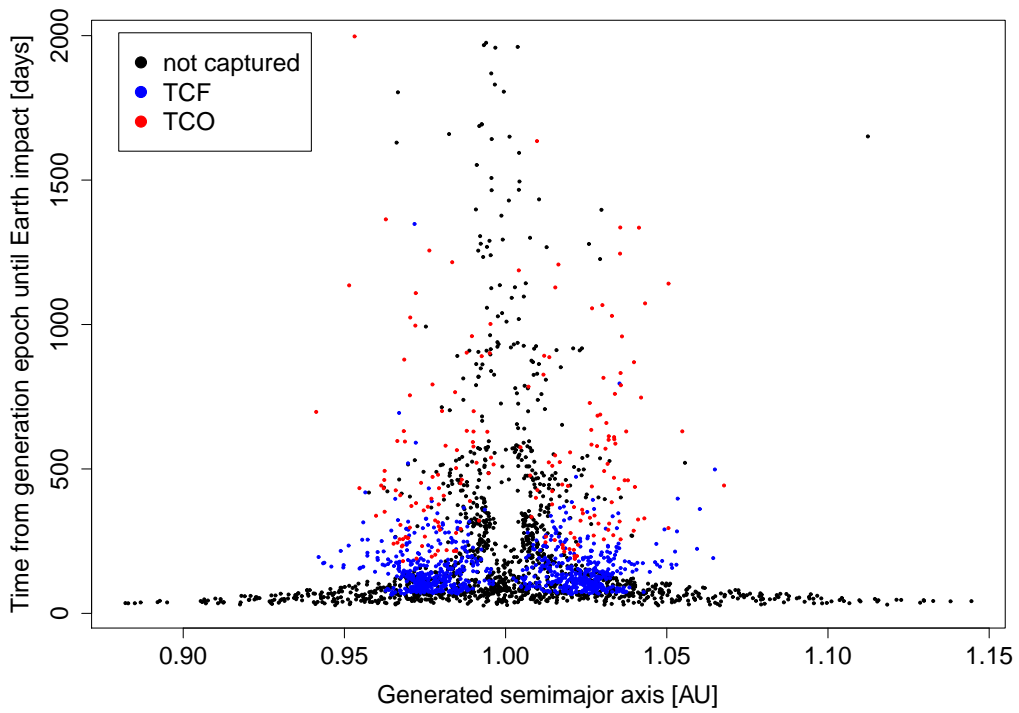


Figure 24: The time from generation epoch to Earth impact as a function of the generated semimajor axis for (red) temporarily-captured orbiters, (blue) temporarily-captured flybys, and (black) uncaptured objects.

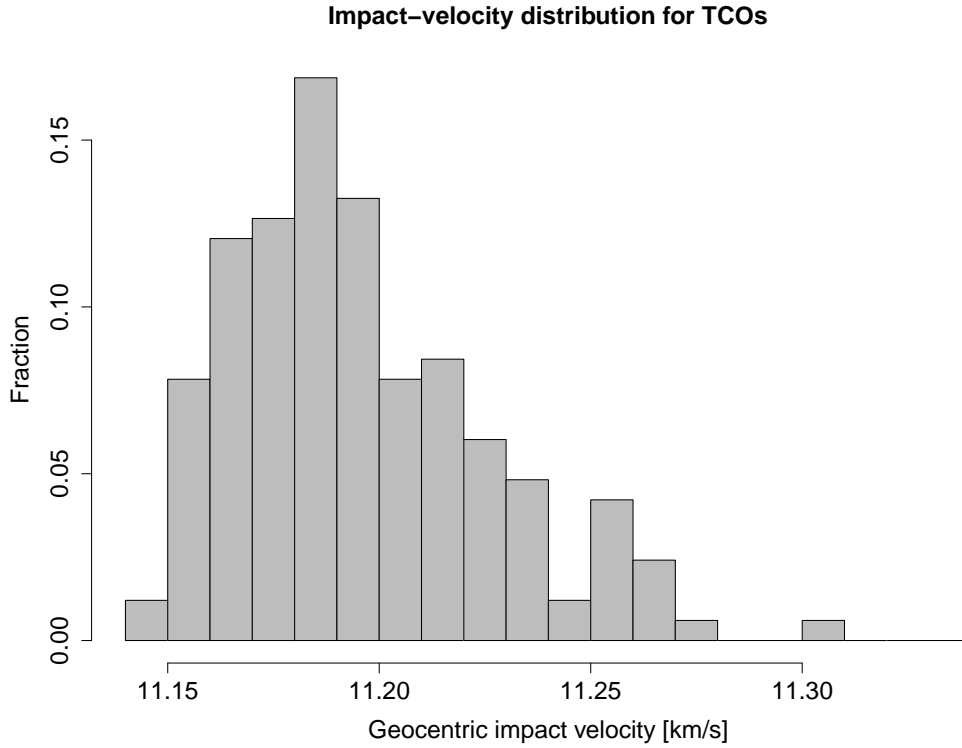


Figure 25: The Earth-impact speed distribution for temporarily-captured orbiters. The Earth’s escape speed is 11.2 km s^{-1} . The Earth-impact speed estimates come from orbital integrations for which the requirement on the relative accuracy was set to 10^{-10} .

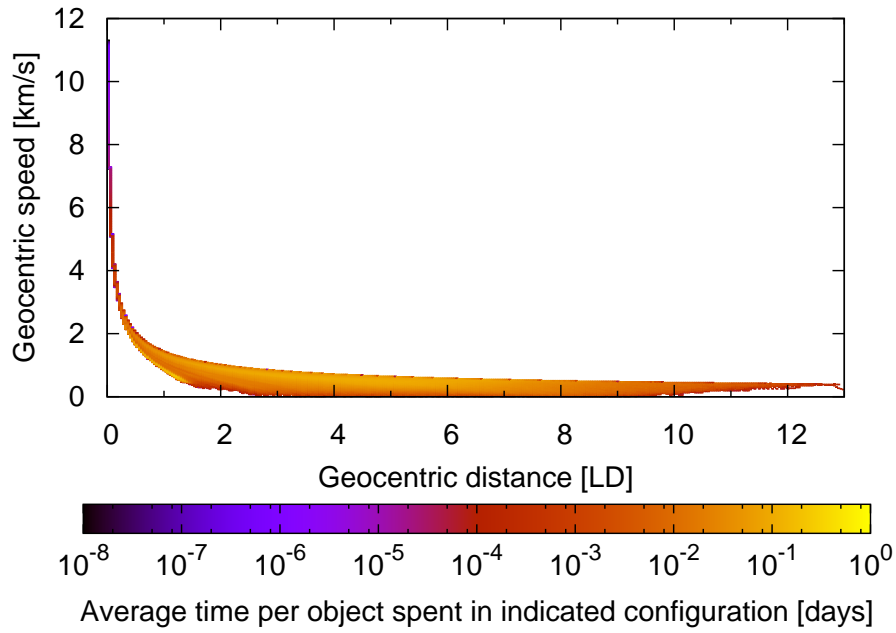


Figure 26: The TCO residence time as a function of geocentric (r_g, v_g) . The implication is that TCOs will be difficult to detect from the ground because they are moving fast when they are closest to the Earth and thus at their brightest.

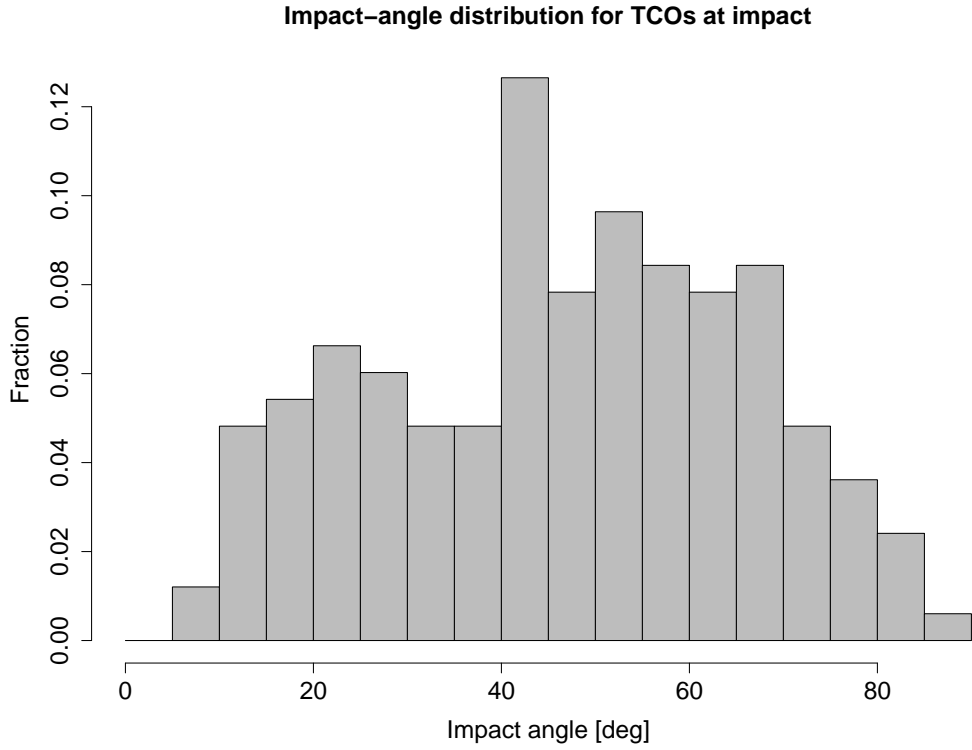


Figure 27: Impact-angle distribution for Earth-impacting temporarily-captured orbiters at the time of hitting the Earth's surface.

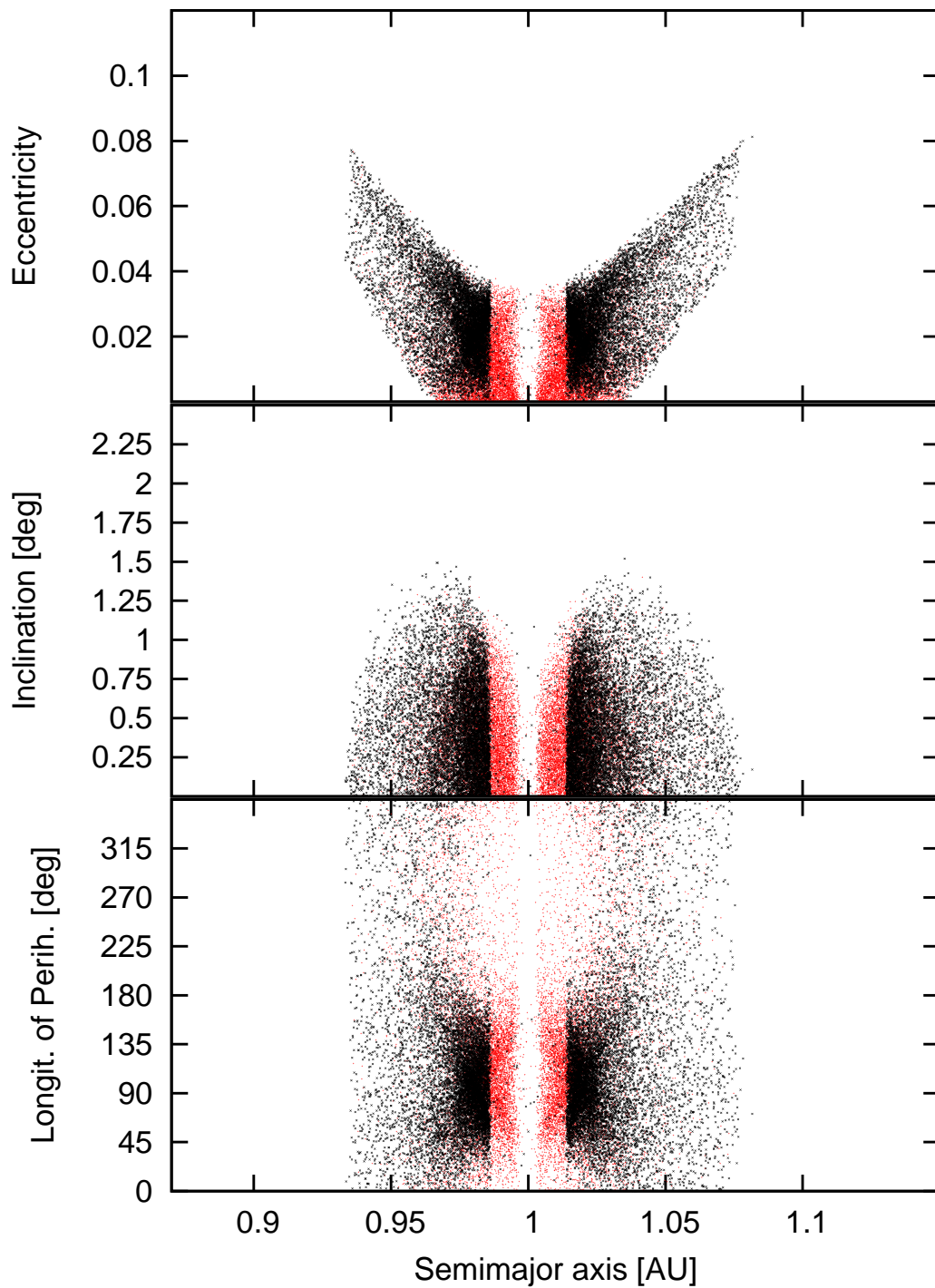


Figure 28: (black) Orbital elements for temporarily-captured orbiters one year after their escape from the EMS⁵⁹ and (red) the same objects' elements prior to capture.

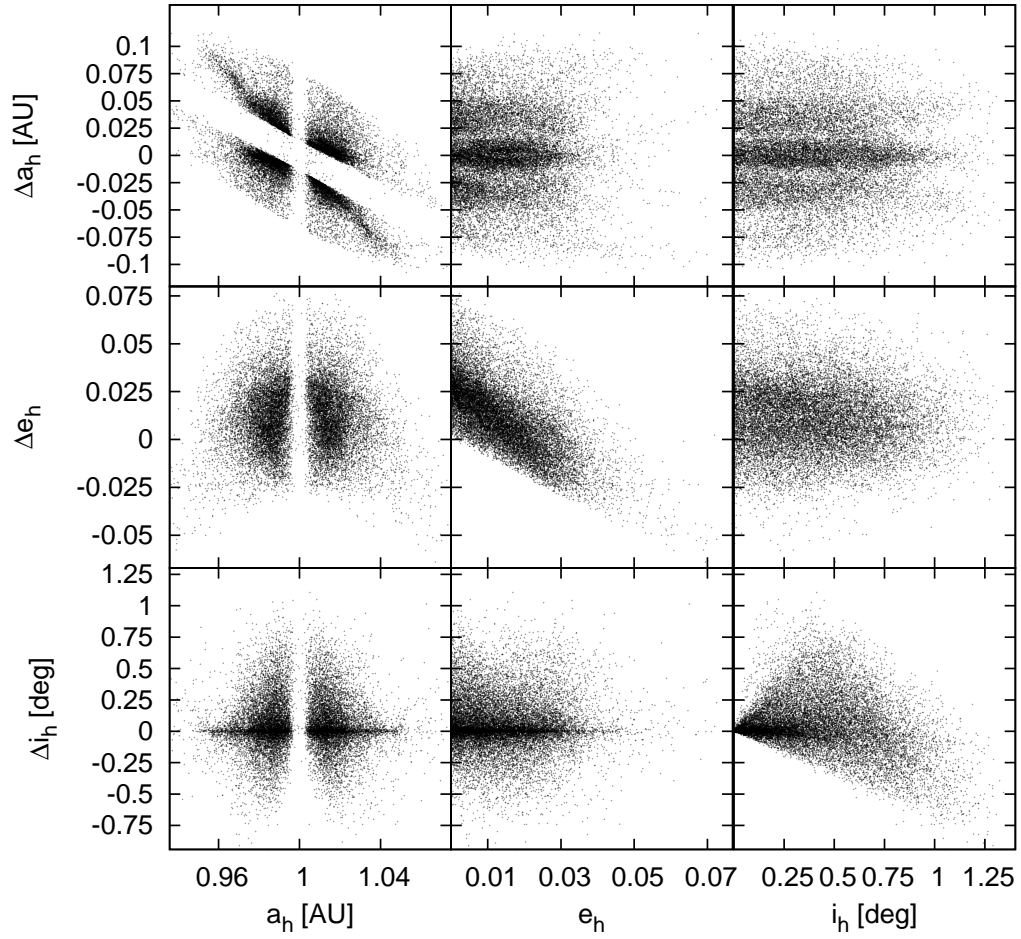


Figure 29: The change in orbital elements for temporarily-captured orbiters between the generation epoch (prior to capture) and the epoch one year after the escape from the EMS.

A A method for computing a 6D orbit given (a, e, i) and a position vector \mathbf{r}

In this work the generation of the ‘intermediate source population’ requires that we generate NEOs with a known (a, e, i) distribution within a shell from 4-5 Hill radii of the Earth. Here we present an analytical technique for generating these objects rather than the ‘brute-force’ technique employed above.

Given (a, e, i) and the position vector from the central body to the object of interest at epoch t_0 $\mathbf{r}(t_0) = (x, y, z)_{t_0}$ to calculate the corresponding 6D orbit we need to solve for either $\dot{\mathbf{r}}(t_0)$ or (Ω, ω, M_0) , where Ω is the longitude of ascending node, ω is the argument of pericenter, and M_0 is the mean anomaly at the chosen epoch. In what follows we solve for the latter as this choice results in a more elegant method.

An object’s cartesian coordinates in the orbital plane at the epoch time, $\mathbf{r}_p(t_0) = (x_p, y_p, z_p)_{t_0}$, are given by

$$\begin{aligned} x_p &= a(\cos E - e), \\ y_p &= a\sqrt{1 - e^2} \sin E = a\sqrt{(1 - e^2)(1 - \cos^2 E)}, \\ z_p &= 0, \end{aligned} \tag{14}$$

where E is the eccentric anomaly and

$$\cos E = \frac{1 - \frac{|\mathbf{r}|}{a}}{e} \tag{15}$$

Combining Eq. 15 and Kepler’s equation yields two possible values for M_0 .

The coordinates in the orbital plane $\mathbf{r}_p(t_0)$ are connected to the coordinates in the ecliptic plane $\mathbf{r}(t_0)$ through the 3×3 rotation matrix R

$$\mathbf{r}(t_0) = R\mathbf{r}_p(t_0), \tag{16}$$

with

$$\begin{aligned}
R_{11} &= \cos \Omega \cos \omega - \sin \Omega \sin \omega \cos i \\
R_{12} &= -\cos \Omega \sin \omega - \sin \Omega \cos \omega \cos i \\
R_{13} &= \sin \Omega \sin i \\
R_{21} &= \sin \Omega \cos \omega + \cos \Omega \sin \omega \cos i \\
R_{22} &= -\sin \Omega \sin \omega + \cos \Omega \cos \omega \cos i \\
R_{23} &= -\cos \Omega \sin i \\
R_{31} &= \sin \omega \sin i \\
R_{32} &= \cos \omega \sin i \\
R_{33} &= \cos i .
\end{aligned} \tag{17}$$

Combining Eqs. 14–17 we derive the following separate equations for $\cos \Omega$ and $\cos \omega$

$$A_{\Omega} \sqrt{1 - \cos^2 \Omega} - \cos \Omega + B_{\Omega} = 0, \tag{18}$$

$$A_{\omega} \sqrt{1 - \cos^2 \omega} + B_{\omega} \cos \omega - C_{\omega} = 0, \tag{19}$$

where

$$\begin{aligned}
A_{\Omega} &= \frac{x}{y}, \\
B_{\Omega} &= \frac{z}{y \tan i}, \\
A_{\omega} &= a \left(\frac{1 - \frac{|\mathbf{r}|}{a}}{e} - e \right), \\
B_{\omega} &= a \sqrt{(1 - e^2) \left(1 - \left(\frac{1 - \frac{|\mathbf{r}|}{a}}{e} \right)^2 \right)}, \\
C_{\omega} &= \frac{z}{\sin i}.
\end{aligned}$$

B_{Ω} and C_{ω} have singularities at $i = 0^\circ$ that correspond to Ω and ω being undefined for zero-inclination orbits. Similarly, A_{ω} and B_{ω} have singularities at $e = 0$ that correspond to ω being undefined for circular orbits. B_{Ω} also has a singularity at $y = 0$.

The solutions to Eqs. 18 and 19 are simply obtained from the quadratic equation:

$$\cos \Omega = \frac{B_\Omega \pm A_\Omega \sqrt{A_\Omega^2 - B_\Omega^2 + 1}}{A_\Omega^2 + 1}, \quad (20)$$

$$\cos \omega = \frac{B_\omega C_\omega \pm A_\omega \sqrt{A_\omega^2 + B_\omega^2 - C_\omega^2}}{A_\omega^2 + B_\omega^2}. \quad (21)$$

The right-hand sides of Eqs. 20 and 21 have a non-zero imaginary part if i) the pericenter distance $q = a(1 - e)$ is larger than $|\mathbf{r}(t_0)|$, ii) the apocenter distance $Q = a(1 + e)$ is smaller than $|\mathbf{r}(t_0)|$, and/or iii) the z -component of the position vector is larger than $|\mathbf{r}(t_0)| \sin i$. Since solutions with non-zero imaginary parts are non-physical, we choose only the real valued solutions and determine which permutations of $(a, e, i, \Omega_j, \omega_k, M_{0,m})$, where $j = 1, 2, 3, 4$, $k = 1, 2, 3, 4$, $m = 1, 2$, result in

$$|\mathbf{r}(t_0) - \text{pos}(a, e, i, \Omega, \omega, M_0, t_0)| < \epsilon, \quad (22)$$

where the operator pos converts Keplerian elements to a Cartesian position, and ϵ is a small positive quantity. For a given combination of a, e, i and $\mathbf{r}(t_0)$ we get either zero or four orbits (cf. Jedicke 1996).